



Sara Cristina Pereira Fonseca

Bachelor of Sciences in Biomedical Engineering

**Evaluation of atherosclerotic plaques
with nano-probes for intravascular
cardiological imaging diagnosis**

Thesis to obtain a Master Degree in
Biomedical Engineering

Advisers:

Dr. Mariana Carvalho,
Research Engineer

International Iberian Nanotechnology Laboratory

Professor Dr. Pedro Vieira,
Assistant Professor

Faculty of Science and Technology, NOVA University of Lisbon

September, 2019

Evaluation of atherosclerotic plaques with nano-probes for intravascular cardiological imaging diagnosis

Copyright © Sara Cristina Pereira Fonseca, Faculdade de Ciências e Tecnologia, Universidade NOVA de Lisboa.

A Faculdade de Ciências e Tecnologia e a Universidade Nova de Lisboa têm o direito, perpétuo e sem limites geográficos, de arquivar e publicar esta dissertação através de exemplares impressos reproduzidos em papel ou de forma digital, ou por qualquer outro meio conhecido ou que venha a ser inventado, e de a divulgar através de repositórios científicos e de admitir a sua cópia e distribuição com objetivos educacionais ou de investigação, não comerciais, desde que seja dado crédito ao autor e editor.

The important thing is to not stop questioning.

Curiosity has its own reason for existing.

Albert Einstein

Firstly, I would like to sincerely thank my advisors Dr. Mariana Carvalho and Prof. Dr. Pedro Vieira for their advice and dedication to this project for the past 6 months. To Dr. Mariana Carvalho for the opportunity of contributing to a project with such a significant impact in our daily lives, for the freedom on exploring new approaches and for the constant availability. To Prof. Pedro Vieira, for his endless dedication and support, for always motivating me to go further, permanent peace of mind even in the stormiest days and for the unique way of always turning a difficulty into a challenge. To both I am extremely grateful.

To the INL staff thank you for creating an excellent work environment, for giving me the tools for developing the best work possible and for giving me such happy memories.

To my lab partner, João Vieira, thank you for showing me peace in the middle of the storm and for the support throughout the long hours we spent together in this project. To the craziest housemates, the funtastic four, Pedro, Rodrigo, Tó, and João Vieira for making me laugh every single day for the past six months. This adventure would have never been the same without you. Also, to Bia for being the sixth member of our home and always having a huge hug for me. Braga will always have a special place in our hearts.

To my second family, the FCT family thank you for making this 5 years unforgettable. To DDN, Inês, Marta, Bruna and Leonor, thank you for the longing videocalls that made me smile in the lonely days, for the memories around the world and for the amazing journey our friendship has been. To Sol, thank you for being by my side since the first day of this journey and for the endless memories. To Bia, Cris, Dô and Beatriz for choosing me to guide you in this journey and for the unique love. To João Tavares, the best friend that FCT gave me. Thank you for understanding me so well and for showing me that love comes in many forms. To Ruca, for the patience and help in the most difficult times, thank you for being so supportive. To Tó, thank you for your motivational speeches and meaningful words, for always being present and for being so caring with our friendship.

To the sisters, not by blood but by love, Marta and Cati thank you for, even miles apart, supporting me and showing me true friendship and love.

To Lela, Pedro, João, Gaby and Luis, thank you for showing me that family is love, family is support and mostly friends are the family we choose.

To Bruno, whose love and care helped me to get through difficult times. With all my heart thank you for staying by my side and never giving up on me, for showing me the sky was not the limit and for all our polaroid memories.

Este último parágrafo será escrito em português porque as pessoas nele mencionadas merecem algo especial.

À minha mãe, a maior força da Natureza que conheço. Obrigada pelo exemplo de superação que sempre foste para mim. Obrigada por teres sempre acreditado em mim mesmo quando eu própria não acreditava.

Ao meu pai, o maior génio que conheci. Obrigada por me contagiares com essa vontade de viver que me motiva em todas as alturas a ser melhor. Obrigada por nunca me teres deixado desistir dos meus sonhos. São os meus ídolos, o meu abrigo e agradeço-vos por todas as oportunidades que nunca me foram negadas.

Cardiovascular diseases represent the leading cause of mortality and disability worldwide. Besides, it is estimated that these numbers will increase significantly in the future. More specifically, atherosclerosis is present in most of the main cardiovascular diseases, making its study urgent and important to develop new diagnostic tools.

The most relevant limitation in the current investigation of the evaluation of atherosclerosis is the impossibility to distinguish stable and prone to rupture (unstable) plaques in coronary arteries. Associated with the instability phenomena, in plaques prone to rupture, are increased thickness of tissue layers (already detectable but not provide an unequivocal diagnosis) and inflammatory processes (not yet detectable but only present when the lesion evolves higher risk to rupture).

Aiming to detect the precise location of inflammatory processes, two types of contrast agents (nano probes) were synthesized, gold nanoparticles and microbubbles. Also, to replicate the behavior of human arteries, three-dimensional tissue simulating structures (phantoms) were fabricated and optimized.

To evaluate the performance of the contrast agents, both in the phantoms and post-mortem human arteries, optical coherence tomography (OCT) images were acquired in a clinical environment, and other techniques were performed (confocal microscopy, scanning electron microscopy, atomic force microscopy) to characterize the samples.

Microbubbles revealed to be a better contrast agent than gold nanoparticles having a clearly noticeable enhancement of the OCT signal. After the acquisition of several OCT images on both types of samples (arteries and phantoms) an automatic imaging processing software was developed to detect the presence of the contrast agents and its posterior location.

The software uses MATLAB as a programming language and with a user-friendly interface the user can access numerous parameters of the analyzed image and even edit them manually. In the end of the automatic processing, the user has the information of the number of regions of interest as well as their visual location.

Key words: atherosclerosis, inflammation, contrast agents, optical coherence tomography, imaging processing software

As doenças cardiovasculares constituem a principal causa de morte a nível mundial e estima-se também que esses números aumentem de forma significativa num futuro próximo. Mais especificamente, a aterosclerose está presente na maioria das principais doenças cardiovasculares, tornando-se cada vez mais urgente o estudo da sua evolução para o desenvolvimento de novas ferramentas de diagnóstico. A limitação mais significativa na avaliação da aterosclerose é a impossibilidade de distinguir entre as placas ateroscleróticas estáveis e as que apresentam elevada propensão para romper (instáveis) nas artérias coronárias. Associado ao fenómeno de instabilidade, característico de uma placa em risco de romper, ocorrem um aumento da espessura das várias camadas de tecido da artéria (fenómeno já detectável mas que não fornece um diagnóstico inequívoco) e de processos inflamatórios (ainda não detectáveis, mas presentes apenas quando a lesão evolui para maior risco de ruptura).

Com o objetivo de detectar a localização precisa dos processos inflamatórios nas artérias, foram sintetizados dois tipos de agentes de contraste, nanopartículas de ouro e microbolhas. Além disso, para replicar o comportamento das artérias humanas, foram fabricadas e optimizadas estruturas tridimensionais artificiais, denominadas de fantasmas. Com o intuito de avaliar o desempenho dos agentes de contraste, tanto em artérias humanas post-mortem como nos fantasmas, foram adquiridas em ambiente clínico imagens de tomografia por coerência óptica (TCO). Foram também realizadas outras técnicas (microscopia confocal, microscopia eletrónica de varrimento, microscopia de força atómica) para caracterização das amostras.

As microbolhas revelaram ser um melhor agente de contraste do que as nanopartículas de ouro verificando um aumento claramente visível do sinal de TCO. Após a aquisição de várias imagens de TCO em ambos os tipos de amostras (artérias e fantasmas), foi desenvolvido um software de processamento automático de imagens para detectar a presença dos agentes de contraste e a sua localização.

O software utiliza como linguagem de programação MATLAB e, através de uma interface user-friendly, o utilizador consegue aceder a diversos parâmetros da imagem, bem como editá-los manualmente. Concluído o processamento automático, o utilizador possui a informação do número de regiões de interesse detectadas, assim como a sua localização.

Palavras Chave: Aterosclerose, inflamação, agentes de contraste, tomografia por coerência óptica, software de processamento de imagem

Acknowledgments.....	VII
Abstract.....	IX
Resumo	XI
List of Figures.....	XV
List of Tables	XIX
Glossary	XXI
1. Introduction.....	1
1.1. Context and Motivation.....	1
1.2. State of the Art	1
1.3 Objectives	6
2. Theoretical Concepts.....	7
2.1 Cardiovascular System.....	7
2.2 Development of the Atherosclerotic Plaque.....	8
2.3 Tissue Optical Properties	9
2.4 Contrast Agents	11
2.4.1 Microbubbles (MB)	11
2.4.2 Gold Nanoparticles (GNP).....	13
2.5 Principles of Optical Coherence Tomography (OCT)	13
2.6 Antibody – Properties and functions.....	15
2.7 Confocal Microscopy.....	16
2.8 Atomic Force Microscopy (AFM)	18
2.9 Scanning Electron Microscopy (SEM).....	20
3. Experimental Methods.....	23
3.1 Tissue Simulator Phantom Design	23
3.2 Titanium Dioxide Synthesis (TiO ₂).....	24
3.3 Gold Nanoparticles Synthesis and Immobilization (GNPs).....	25
3.4 Microbubbles Synthesis	28
3.5 Functionalization Methods.....	28

3.6	Immunohistochemistry	29
4.	Phantom Characterization Methods	31
4.1	Confocal Microscopy.....	31
4.2	Scanning Electron Microscopy (SEM).....	33
4.3	Atomic Force Microscopy (AFM)	34
5.	Image Acquisition	35
5.1	Acquisition Methods	35
5.2	Processing Tools.....	38
5.3	Accuracy tests	44
6.	Conclusions.....	49
	References.....	51
	Appendix I – User’s Guide	54

Figure 2.1: Anatomy of the coronary circulation7

Figure 2.2: Cross-section of coronary artery8

Figure 2.3 : Features exhibited by a vulnerable plaque.....9

Figure 2.4: Basic microbubble structure11

Figure 2.5: Comparison of various imaging methods according to their resolutions and penetration depths14

Figure 2.6: Michelson's interferometer basic setup14

Figure 2.7: Antibody basic structure16

Figure 2.8: Schematic representation of laser scanning confocal microscope17

Figure 2.9 : Schematic presentation of AFM.....18

Figure 2.10: Common SEM assembly.....20

Figure 2.11: SEM interactions21

Figure 3.1: Developed phantoms - (a) one-layer clear PDMS (b) one-layer PDMS incorporated with TiO₂.....24

Figure 3.2: Schematic of double layer phantom shaping and the two replicated layers24

Figure 3.3: Solutions before (a) and after (b) magnetic stirring.....26

Figure 3.4: PDMS substrates after oxygen plasma activation. Sample with half the surface exposed to oxygen plasma and half covered.....27

Figure 3.5: Schematic of gold nanoparticles immobilization into the PDMS27

Figure 3.6: Lyophilized VeVo Micromarker stored in a glass vial (a) Schematic representation of non-targeted and target-ready surface modified microbubbles (b) ...28

Figure 4.1: Microbubbles confocal images (1) stock solution (2) 1:4 dilution (3) 1:40 dilution.....31

Figure 4.2: Dried drop of microbubbles' solution showing a clear aggregation of microbubbles on the edge (2) forming an interface between the interior of the drop (1) and the blade itself (3).....	32
Figure 4.3: Interface created showing the difference between functionalization (1) and non-functionalization (2) in the immobilization of gold nanoparticles in the phantom	32
Figure 4.4: SEM images of titanium dioxide acquired commercially (left) and synthesized (right).....	33
Figure 4.5: SEM images of synthesized star-shaped gold nanoparticles	33
Figure 4.6: Histogram presenting gold nanoparticles size distribution	34
Figure 4.7: AFM roughness measurements comparing clear PDMS (average 10.4 nm surface) and PDMS with gold nanoparticle at the surface (average 86 nm	34
Figure 5.1: Original sample preparation to perform OCT measurements	35
Figure 5.2: Complete assembly of an OCT measurement	35
Figure 5.3: Final OCT measurement assembly (left) schematic including arteries and phantoms (right) photograph taken in the moment of an OCT measurement in Hospital de Braga, with a upper vision of the complete assembly with a phantom.....	36
Figure 5.4: Schematic of OCT imaging acquisition mode.....	36
Figure 5.5: Calibration procedures with deionized water (left) and air (right)	37
Figure 5.6: OCT measurements of negative controls with clear PDMS (left) and one-layer phantom of PDMS and TiO ₂ (right).....	38
Figure 5.7: Comparison between the provided signal of gold nanoparticles (left) and microbubbles (right). The yellow arrows show the exact location of the contrast agent	38
Figure 5.8: Identification of the regions of interest both in a phantom (left – region i) and in a human artery (right – regions 1 and 2). The red lines establish the boundaries of each region.....	40
Figure 5.9: Polar coordinates	41
Figure 5.10: Implemented axle system	41
Figure 5.11: Schematic of degree variation and pixel resolution	42

Figure 5.12: Schematic of the analyzed areas by the algorithm (blue) and the ones excluded (black) maintaining the same number of columns in the matrix	42
Figure 5.13: Comparison between 2 types of profiles. Profile A presenting and homogenous distribution of scattering and profile B presenting a shadow and a well-defined intensity peak.....	43
Figure 5.14: Difference in profiles where Profile A represents a generic region and Profile B represents the location of a contrast agent.....	44
Figure 5.15: Detection of regions of interest in calibration measurements. phantom without microbubbles (left) and water (right).....	44
Figure 5.16: Correct detection of region of interest in phantom	44
Figure 5.17: Partial detection of region of interest in phantom (left) and zoom in the breach (right).....	44
Figure 5.18: Correct detection of region of interest in phantom after eliminating the pre-existing breach	44
Figure 5.19: Partial detection of region of interest in human artery.....	44
Figure 5.20: Partial detection of region of interest in human artery.....	44
Figure 5.21: Incorrect detection of region of interest in human artery	44
Figure I.1: Overall view of the interface	544
Figure I.2: Original image and corresponding histogram of reference	55
Figure I.3: Processed image with increased brightness and corresponding histogram	55
Figure I.4: Processed image with increased contrast and corresponding histogram	55
Figure I.5: Processed image with gamma < 1 and corresponding histogram.....	56
Figure I.6: Automatic detection of regions of interest (1 – left and 0 right).....	56
Figure I.7: Activation of editable parameteres by manual detection.....	57
Figure I.8: Example of a crop and zoom in the analyzed image.....	57
Figure I.9: Overall view of the auxiliary interface for reference.....	58
Figure I.10: Pop up message and corresponding reference image	58
Figure I.11: Report generated after running the algorithm.....	59

Table 2.1: Healthy coronary artery behavior to NIR light [Adapted from [19]].....	10
Table 2.2: Vantages and disadvantages of laser scanning confocal microscopy.....	17
Table 2.3 : AFM modes.....	19
Table 2.4: Advantages and disadvantages of SEM technique.....	21

ACS	Acute Coronary Syndrome
AFM	Atomic Force Microscopy
CT	Computerized Tomography
CVDs	Cardiovascular Diseases
GE-CMR	Gadofosveset-enhanced cardiac magnetic resonance
GNPs	Gold Nanoparticles
GNR	Gold Nanorods
GNS	Gold Nanoshells
IV-OCT	Intravascular Optical Coherence Tomography
IVUS	Intravascular Ultrasound
LCA	Left coronary artery
LSPR	Localized surface plasmon resonance
NIR	Near infrared
oxLDLs	Oxidized LDL
PDMS	Polydimethylsiloxane
PET	Positron Emission Tomography
RCA	Right coronary artery
SEM	Scanning electron microscopy
SERS	Surface-enhanced Raman Scattering
SMC	Smooth Muscle Cells
TCFA	Thin Cap Fibroatheroma

1. Introduction

1.1. Context and Motivation

Cardiovascular diseases (CVDs) are currently the leading cause of mortality and disability worldwide^[1] and not only in industrialized countries like in 2002^[2]. The numbers are overwhelming, and it is estimated that by the year 2030, 23.3 million people will die from CVDs.

CVDs can be separated into five groups^[1], with the following characteristics:

- Coronary heart disease occurs when a plaque/blood clot blocks the coronary blood flow;
- Stroke appears when there is not enough oxygen reaching the brain due to a blocked blood vessel;
- Peripheral arterial disease occurs when a plaque/blood clot blocks the blood flow supplying arms and legs;
- Aortic aneurysms are defined as arterial enlargement with loss of arterial wall parallelism;
- Deep vein thrombosis occurs when a blood clot is formed in the deep leg vein.

From the five diseases presented above, three of them (coronary heart disease, stroke, and peripheral arterial disease) involve atherosclerosis as the primary cause of underpinning CVDs^[1].

The rupture of vulnerable atherosclerotic plaques is responsible for about half of the diagnosed cases of acute coronary syndromes; however, conventional methods cannot identify when a plaque is prone to rupture^[2]. As so, it is urgent to understand the mechanisms that lead to plaque instability as well as the inflammatory process behind the plaque evolution in order to predict the moment of rupture in high-risk plaques.

1.2. State of the Art

According to the literature (list of references), atherosclerosis is defined as *a multifactorial and slowly progressing disease in large and mid-sized arteries characterized by a disturbed blood flow dynamics*^[1].

The evolution of atherosclerosis is considered a dynamic process where early and stable lesions (fibroatheroma) prograde to advanced and unstable plaques (thin cap fibroatheroma – TCFA)^[3]. It is known that more than two-thirds of acute coronary events, a consequence of coronary heart disease, are associated with plaque erosion or rupture^[3]. As so, it is essential to

understand the clinical events and mechanisms associated with the transition to vulnerable lesions as well as to define plaque characteristics in the several stages of the disease. The index manifestation of atherosclerotic disease is an intimal xanthoma^[3], characterized as an accumulation of smooth muscle cells, originating a deposit rich in cholesterol, without the presence of inflammation.

According to the American Heart Association, the first distinguishable plaque is fibroatheroma, a stable plaque composed by a lipid-rich necrotic core surrounded with fibrotic tissue^[3]. Fibroatheroma is divided into two stages, characterized by:

- Early-stage, where macrophages start to infiltrate in the lipid pool;
- Late-stage, where the increased amounts of free cholesterol and the depletion of the extracellular matrix can result in luminal stenosis, due to episodes of intraplaque hemorrhage.

Fibroatheroma usually evolves to thin-cap fibroatheroma (TCFA) which is already considered a vulnerable atherosclerotic plaque with high-risk to rupture. However, vulnerability is much more connected with an inflammatory process than with the plaque morphology itself. As so, it is even more urgent to characterize the molecular profile of atheromas in order to understand the inflammatory process^[4]. The signature of TCFA is a thin and inflamed fibrous cap overlying a large lipid pool^[5]. The necrotic core of the plaque is considered large since it occupies more than 25% of the plaque area, and macrophages massively infiltrate it. An essential precursor to plaque rupture is the weakening of the fibrous cap. When the necrotic core occupies more than 30% of the plaque area, and there is luminal thrombus formation, TCFA evolves into ruptured plaque^[3]. The thrombus results from the infiltration of inflammatory cells within the elements of the extracellular matrix.

Several studies showed that in patients diagnosed with acute coronary syndrome (ACS), the presence of plaque rupture is the most frequent and most significant event causing a lesion^[3]. As so, it is the fibrous cap thickness that discriminates between TCFA (intact thin fibrous cap vulnerable to rupture) and fibroatheroma (thick fibrous tissue)^[3].

Initially, coronary plaques are not detectable in coronary angiography because they do not cause hemodynamically stenosis^[6]. Coronary angiography is a cardiovascular imaging technique used in diagnosis or therapy guidance after diagnosing atherosclerosis^[1]. This technique provides 2D imaging of blood vessels with a high spatial resolution. Moreover, it presents some limitations that difficult the discrimination between the two natures of the atherosclerotic plaques: low sensitivity, exposure the patient to radiation and possible allergies to iodinated contrasts^[1]. Also, the most significant limitation of this technique is, due to the remodeling of the vessels, the insensitivity to quantify plaque and thrombus burden, a critical

predictor of ACS^[7].

One of the most common and with a higher degree of precision of noninvasive imaging techniques is Computerized Tomography (CT). Since CT has an excellent spatial resolution (50 – 200 μm) and deep tissue penetration, it allows fast 3D anatomic images. Although used worldwide, the need for iodinated contrast agents in several diagnoses represents a limitation for CT imaging. The main reasons are:

- Impossibility to conjugate the contrast agent with biological markers for specific targets;
- Short imaging window due to the rapid clearance of the contrast agent by the kidney.

A recent study using CT imaging^[1] tried to track the recruitment of monocytes, which is one of the first steps in the development of the atherosclerotic plaque, in order to evaluate the evolution of the coronary lesion. It is essential to comprehend how the inflammatory process begins and as so, which cells are recruited to the development of the plaque.

A study published by the American College of Cardiology^[6], using Gadofosveset-enhanced cardiac magnetic resonance (GE-CMR), demonstrated for the first time the noninvasive detection of coronary lesions and TCFA present in the coronary arteries. Gadofosveset was the first intravascular contrast approved for biological use and its accumulation within the matrix of atherosclerotic plaque makes it a suitable marker of endothelial permeability^[6]. Since it is a gadolinium-based probe, the use of ionizing radiation represents its major limitation. The use of targeting probes in molecular imaging represents innovative possibilities to better understand the stages of plaque formation as well as early diagnosis of atherosclerosis. In the mentioned study, TCFA was considered as a vulnerable plaque when cap thickness was less than 65 μm , and the lipid core had an arc more than 90° degrees. Image analyses, in patients previously diagnosed with ACS, showed a significantly higher signal enhancement after contrast application, allowing the identification of TCFA with high diagnostic accuracy. Three significant limitations were identified in the present study^[6]:

- A long scan time to be used in a clinical environment (32 minutes);
- Misregistration errors due to the fusion of data sets (from CMR angiography and vessel wall imaging sequence) and respiratory pattern;
- Impossibility to identify TCFA in plaques containing severe calcification.

Recently, surface-enhanced Raman scattering (SERS) was used with the same purpose to detect inflammation^[1] and consequently, determine plaque instability. SERS is a spectroscopic nonlinear optical technique which detects biomolecules with an outstanding capacity. The significant limitations of the technique are due to the limited depth and sensitivity (minimal molecular cross-section) as well as long scanning times. Although the presence of some limitations, it was possible to detect ICAM-1, a protein that is expressed by endothelial cells

when inflammation is present^[1].

Since inflammation increases cell metabolic activity, studies using positron emission (PET)^[8] were able to identify glucose utilization, and as so detecting lesion vulnerability due to inflammation. However, this technology presents some limitations that do not make it suitable for clinical diagnosis of high-risk atherosclerotic plaques:

- Poor spatial resolution;
- Respiratory and cardiac motion difficulties accurate localization of plaque inflammation;
- Background noise due to glucose consumption by the myocardial muscle.

In order to fill the limitations of the techniques mentioned above, some studies started to apply Optical Coherence Tomography (OCT) in cardiovascular disease diagnosis, instead only in ophthalmological context to retinal imaging^[1]. Intravascular OCT's high sensitivity allows discrimination between three types of plaques^[8]:

- Fibrous, which has a high and homogenous backscattering signal^[5];
- Fibrocalcific, which shows a weak signal due to the presence of calcification^[5];
- Lipid-rich, which have poorly delineated borders and lipids are present for more than 90° in any cross section^[5].

Its major limitation is due to limited tissue penetration (1 – 3 mm) that does not allow a complete reflection of light from the deeper arterial layers^[3].

In comparison to intravascular ultrasound (IVUS), which has the same principle of operation, OCT exceeds by one order of magnitude the spatial resolution of the equipment, allowing more precise measurement of the cap thickness, but cannot penetrate as far as the IVUS. Currently, OCT is the only imaging technique with enough resolution to measure in a precise way the fibrous cap thickness^[5], one of the characteristics to distinguish plaque vulnerability, but not in an unequivocal way. Although the significant advantages and progress brought by OCT systems, a reliable assessment at plaque level^[3] and, as a consequence, the discrimination between high-risk and stable plaques is not yet possible.

One of the limitations transverse to all of the techniques reported above is the lack of contrast enhancement in the characterization of vascular layers^[1] and as so the identification of changes through time within the atherosclerotic plaques. In order to solve this limitation, several studies using metallic nanoparticles^[9], especially gold nanoparticles (GNPs), are being done to improve the diagnosis of high-risk plaques.

Gold nanoparticles are proved to scatter light very efficiently^[1] depending on their size and shape^[9] and represent an excellent alternative to endogenous materials (like proteins or types of cells already existing in the human body), which present the following limitations^[9]:

- High cost;
- Low photostability, essential when working with OCT;
- Difficulty in tuning into de NIR region (the region on where the OCT operates).

Metallic nanoparticles present high photostability and can be tuned into the NIR region by changing particle morphology^[9]. Also, gold nanoparticles present specific characteristics^[9] that makes them suitable to fill the limitations of the endogenous materials presented above:

- Biocompatibility;
- The possibility of functionalization to target specific biomarkers of cells mechanisms;
- Increased contrast in OCT images;
- Plasmon resonance wavelength not far from 1300 nm, the wavelength operating in the OCT equipment^[10].
- Easily synthesized;
- Inert.

Not all geometries allow a better contrast improvement in OCT images. As so, spheres, cages, and rods were proved not to be the best shape of GNP since their plasmon band does not match the central wavelength of the IV-OCT^[9]. The same study showed that stars and branched GNPs provided a reliable and very efficient light scattering, making them suitable candidates for contrast agents^[9]. Nevertheless, the best contrast enhancement for clinical OCT equipment was obtained using gold nanoshells (GNS)^[1]. When compared to gold nanorods (GNR), GNS present scattering cross-sections two orders of magnitude above GNR^[10] and a much broader spectrum. The concentration of the GNP varies inversely with the obtain signal^[1], as it is only possible to visualize different spikes of GNS in the image at low concentrations^[10]. Also, GNS resonate in the NIR region, where clinical OCT system usually operates. The limitation reported to this type of GNP is the possibility of a nonuniform distribution of GNS in the plaque may induce false diagnosis^[1].

Although nanoparticles present enormous advantages, toxicity concerns in the biological environment need to be taken into account due to potential health risk^[11]. The toxicity results from the potential interference of the nanoparticles with vital cellular functions due to the similar size between nanoparticles and organelles. One of the most important factors to take in consideration is size since nanoparticles larger than 9 nm are retained in liver and kidneys^[11], which makes them toxic and may cause many side effects^[12]. Nanoparticles can also react with other metals in the bloodstream or produce free radicals, which induces oxidative stress, inflammation, or even cell destruction^[11]. Another limitation with gold nanoparticles is the leakage to the surrounding tissues, which decreases contrast^[12].

Interestingly, microbubbles are biocompatible particles already used as contrast agents for

ultrasound imaging, which have also been demonstrated to act as OCT contrast enhancers^[13]. Currently, and after experiencing significant progress since firstly produced in 1990, it is already possible to produce a broad size distribution^[14] from 1 to 20 μm diameter. Relatively to particle size, it has already been established both upper and lower limits^[15]. In order to avoid embolic events, the maximum diameter that the microbubble should have is between 3 and 5 μm ^[15]. The lower limit is defined by the Rayleigh scattering, where the scattering produced by a particle is proportional to the sixth power of its diameter^[15]. Shell stability has also already been studied, since there are several materials available, and it has been proved bubbles float and remain stable in aqueous media^[15]. Biocompatible and biodegradable polymers used in surgical sutures^[15] have chemical structures similar to those that compose the microbubble's shell.

As so, the next step will be identifying molecular activities within the OCT images due to functionalizing inflammation biomarkers previously identified^[15]: over-expressed selectins (both E and P), vascular cell adhesion molecule (VCAM-1) and intracellular adhesion molecule (ICAM-1).

1.3 Objectives

This project aims to detect the inflammation regions in the arteries through the analysis of OCT images (morphological information) and molecular labeling (biomarkers). As so, it will be necessary to develop:

- Methods of synthesis and functionalization of contrast agents, to optimize signal acquisition and cell targeting;
- Methods of immunochemistry using an emulator of the human arteries in vivo conditions (temperature and circulation), immunofluorescence and molecular labeling;
- Acquisition of images imaging using different techniques of microscopy (scanning electron microscopy, atomic force microscopy and confocal optical microscopy), in order to maximize the acquired signal;
- Acquisition protocol to process optical coherence tomography images (OCT);
- Automatic algorithm to extract information of OCT images and validate the use of contrast agents in human arteries.

2. Theoretical Concepts

2.1 Cardiovascular System

The cardiovascular system consists of the heart (the body's hardest-working organ), blood vessels, and the blood that vessels transport. Throughout the blood flow, it is the system responsible for transporting oxygen, nutrients, hormones, and cellular waste products. In order to pump the approximately 5 liters of blood that circulate in the human body, the heart needs to be adequately supplied with oxygen, which is assured by the two main coronary arteries (left coronary artery and right coronary artery)^[16].

Coronary arteries branch off from the base of the aorta and encase the surface of the heart with smaller vessels that penetrate the walls of the heart and provide the oxygenated blood, necessary to the dynamic behavior of the heart^[16].

According to the figure below (Figure 2.1) is possible to analyze the different ramifications of both left (LCA) and right (RCA) coronary arteries. On average, each main coronary artery is 2 to 4 mm wide.

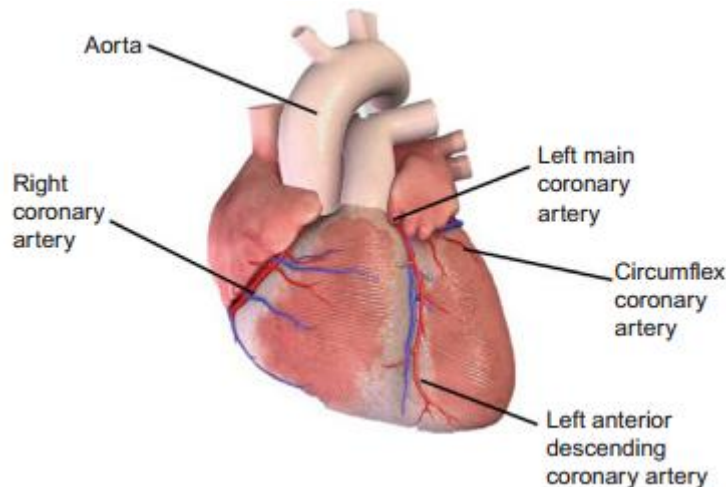


Figure 2.1: Anatomy of the coronary circulation

Adapted from [16]

On the one hand, LCA divides into two main branches (left anterior descending and left circumflex) which are responsible for supplying: two-thirds of the interventricular septum, majority of the left ventricle, left atrium, posterior parts of the left ventricle, back of the heart. On the other hand, RCA and its numerous ramifications are responsible for supplying: right ventricle, right atrium, sinoatrial, and atrioventricular nodes.

The coronary artery wall is divided into three layers^[16] that are composed of different types of cells as it is possible to confirm in the figure below (Figure 2.2):

- Intima, is the inner layer, mainly composed of endothelial cells and connective tissue is responsible for coating the luminal surface of the artery;
- Media, is the middle layer, composed by connective tissue and smooth muscle cells are responsible for maintaining the capability of the artery to expand and contract;
- Adventitia, is the outer layer, composed by fibrous tissue to provide support to the artery.

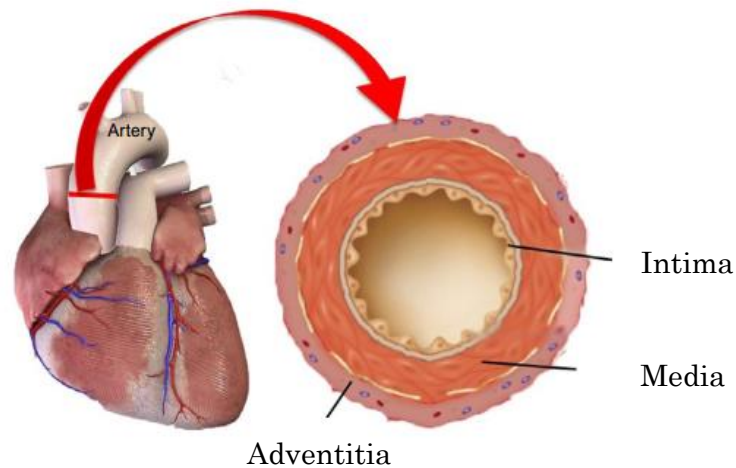


Figure 2.2: Cross-section of coronary artery
Adapted from [16]

2.2 Development of the Atherosclerotic Plaque

Atherosclerosis is mainly characterized by a chronic inflammatory process^[17] in large and mid-sized arteries initiated by cell dysfunction in the arterial wall, where lipoproteins undergo modifications leading to the formation of oxidized LDL (oxLDLs) cholesterol molecules. The newly formed molecules induce the inflammatory process manifested by the recruitment of monocytes. As so, monocytes penetrate subendothelial space and differentiate into macrophages that will recognize the oxLDSs and will start to ingest them^[1].

In an advanced atherosclerotic plaque, cytokines will promote smooth muscle cells (SMC) proliferation that will participate in the fibrous cap development. When SMC die, the necrotic core is formed within the plaque and promote an even more inflammatory environment characterized by defective and fragile blood vessels^[1]. The contact between the necrotic core and blood vessels induce luminal thrombosis that can lead to myocardial infarction and stroke. It is possible to resume the pathological mechanisms of plaque instability^[3] in four related steps:

- Extensive remodeling of the necrotic core with macrophage infiltration;
- Increased inflammation of a thin fibrous cap, without thickening of the cap;
- Increased size of the necrotic core;
- Intraplaque hemorrhage.

Figure 2.3 shows the different features that characterize a vulnerable plaque.

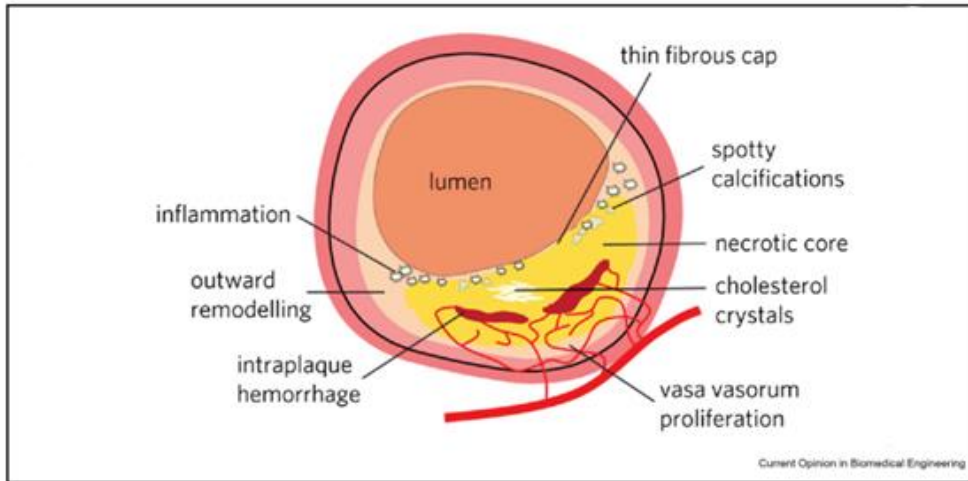


Figure 2.3: Features exhibited by a vulnerable plaque.

Adapted from [17]

When an atherosclerotic plaque is present, the media layer of the artery becomes thinner in ranges between 16 to 190 μm whereas the average thickness of the normal media layer is between 125 and 350 μm ^[16].

2.3 Tissue Optical Properties

The interaction between light and tissue assumes five distinct types: reflection, refraction, absorption, fluorescence, and scattering, and depends on three main factors^[18]:

- Tissue constituents (type of cells, percentage of minerals and water, oxygen saturation);
- Optical properties of each type of tissue;
- Propagation of the light inside the tissue and surrounded medium.

The two most relevant interactions^[19] that contribute to the OCT signal are backscattering and absorption. Backscattering refers to the light scattered and reflected into the tissue^[20] due to the mismatch between the refractive index of tissue constituents and particle size. In tissue, the two types of scattering, Mie and Rayleigh, are mixed.

Referring to the OCT signal, the higher the reflection the brightest the image^[19] becomes, and so does the opposite, darker images are associated with lower values of reflection. Also, fibrous tissue produces higher reflection^[19] (so brighter spots in the image), contrarily to lipidic tissue, which produces darker spots due to lower reflection.

Absorption^[19] refers to the light that penetrates the tissue and is converted into other form of energy, for example thermal radiation. The main absorbers in human tissue in the NIR region are water, hemoglobin, and lipids (most significant plaque component). Referring to the OCT signal, when a high absorption is verified, a shadow appears. Shortly, bright points in images refer to light reflection, and shadows refer to attenuation of the light beam due to reflection or absorption.

Human coronary arteries^[20] present tubular geometry, multilayer composition and since each layer as its behavior (different cells constitution) it becomes possible to compare different behaviors to NIR light to distinguish healthy from atherosclerotic arteries. In table 2.1 is possible to analyze standard measurements already performed in the three layers of a healthy artery.

Table 2.1: Healthy coronary artery behavior to NIR light [Adapted from [20]]

<i>Layer</i>	<i>Area</i>	<i>Reflection signal</i>
<i>Intima</i>	Homogeneous	Strong signal near the lumen
<i>Media</i>	Homogeneous	Low signal
<i>Adventia</i>	Heterogeneous	Strong signal

When analyzing the differences between healthy and diseased arteries, one important parameter to analyze is intimal layer thickening^[19]:

- Physiological thickness $\leq 300 \mu\text{m}$;
- Pathological thickness = $300 - 600 \mu\text{m}$;
- Fibrous plaque thickness $> 600 \mu\text{m}$;
- Thick-cap fibroatheroma $> 600 \mu\text{m}$.

As intimal thickening indicates a probable presence of fibrotic plaque, differences in the OCT signal are verified with the appearance of few shadows^[19] due to the fibrous tissue (note that intimal layer appears bright and homogeneous as previously). Contrarily, when the plaque is composed by lipids^[19], diffuse borders of each layer appear accompanied with strong absorption and low reflection.

In severe atherosclerosis diagnosis, where plaques are always located underneath the cap, fibroatheromas appear in two possible ways^[19], with a difference of $65\mu\text{m}$ in thickness:

- Thick cap, characterized by a sharp border and a dark color, due to low reflection;
- Thin cap, characterized by the presence of shadows with diffuse borders.

Calcifications appear in advanced stages of the disease and are characterized as sharply delineated dark deposits^[19].

2.4 Contrast Agents

In order to develop personalized medical applications, “*molecular imaging probes are being developed to determine the expression of specific molecular markers at different stages of diseases*”^[15]. Also, molecular imaging stands for non-invasive detection and quantification of specific disease receptors which are expressed in the endothelium allowing accurate diagnosis and therapeutic efficacy^[15]. The requirements^[15] needed for a proper contrast agent are presented above:

- Stable on storage;
- Fully biocompatible and biodegradable;
- Easily eliminated from the body with minimal injected dose;
- High detection sensitivity;
- In the case of molecular imaging, ligands need to assure firm adhesion on the targeted vessel wall.

2.4.1 Microbubbles (MB)

Over the past decades, microbubbles have experienced remarkable progress as contrast agents in three main domains^[14]: ultrasound imaging, molecular imaging, and targeted drug and gene delivery. Microbubbles fit as therapeutic agents since they provide a precise location of the contrast (for imaging) as well as specialized functions in drug delivery^[14].

As presented in figure 2.4, microbubbles are composed of gas or air-filled core stabilized with various shell compositions^[21] such as protein, surfactant, lipid, or polymer^[14]. Each microbubble has an average diameter of a red blood cell^[14] (less than 10 μm) to maintain a similar behavior in the blood flow.

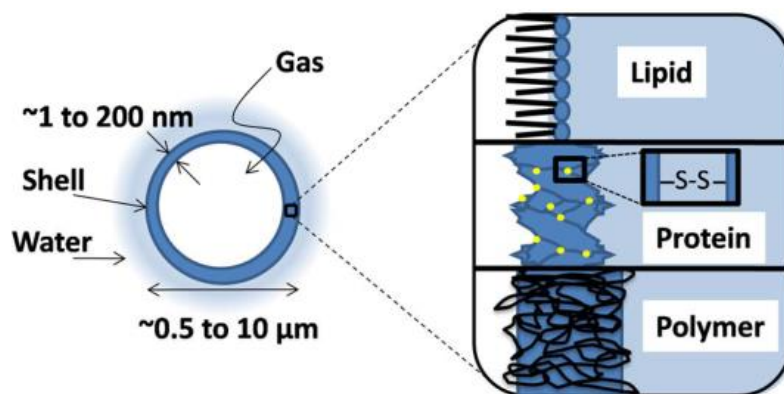


Figure 2.4: Basic microbubble structure

The shell is divided into soft or hard, according to the possibility to be destroyed by ultrasound waves. Soft-shell is used with non-destructive ultrasounds, whereas hard-shell is used with destructive pulses using ultrasound higher frequencies^[21]. Polymeric shells present the following properties^[14], becoming the most suitable for biomedical applications:

- Average thickness of 100 – 200 nm;
- High stability accompanied by low compliance;
- Increased resistance to area compression;
- Variable acoustic pressure, granting the correct location of the microbubble when it is decreased and eliminating the contrast agent through fragmentation when it is increased;

Some of the characteristics that show the potential of microbubbles as an intravascular contrast agent for molecular imaging are:

- their size^[21], since it is too large for extravasation and guarantees that only endothelium is imaged^[14];
- functional aspect^[21] since it allows the quantification of blood flow and blood velocity^[12];
- molecular aspect since it allows the functionalization with anti-bodies that recognize not only inflammatory markers but also cell adhesion molecules (ICAM and VCAM), E and P selectins and $\alpha_v\beta_3$ integrins^[15];
- lifetime between 10 and 40 minutes allowing the possibility to image molecular interactions^[12];
- easily destroyed through a fragmentation pulse^[14].

One of the biomedical applications of microbubbles is imaging the inflamed atherosclerotic endothelium (always present in an atherosclerotic plaque) by modifying the surface of a specific polymer^[21], to allow the recognition of specific inflammatory biomarkers such as E-selectin or VCAM-1.

In order to assure that the microbubble's functionalization correctly recognizes the target (inflammatory markers) it is essential to take into consideration the high specificity of the targeted microbubble and that the chemical modification of the shell facilitates the specific binding. The process of binding the targeted microbubble to activated endothelial cells is evaluated through fluorescence measurements^[21] and is a constant balance between adhesion and flow forces^[15]. The microbubble will remain adherent to the endothelium if the force applied by the blood flow is lower than the adhesion force^[15].

2.4.2 Gold Nanoparticles (GNP)

The primary goal of nanotechnology is to signalize and study the numerous biological processes that occur at the nanometer scale.

Nanoparticles are by definition^[22] *“particles between 1 and 100 nm that have a range of unique properties including surface chemistry, size, shape-dependent electronic, optical properties, bioimaging, vaccine development, biosensors, and therapies.”*

The optical and electronic properties of gold nanoparticles are based on the presence of localized surface plasmon resonance (LSPR) which can be tuned to NIR applications by merely changing the size, shape, surface chemistry, or aggregation state of GNP^[23]. In order to promote bioconjugation, where nanoparticles bond to biomolecules by biological or chemical means, the first ones need to have properties that promote the specific bonding, in particular, rich surface chemistry, low toxicity and be readily synthesized^[9].

2.5 Principles of Optical Coherence Tomography (OCT)

In order to improve diagnosis and to develop innovative therapies, new medical imaging technologies have been advanced over the past decades. Most traditional techniques like MRI, CT or ultrasound, still have an enormous impact in everyday diagnosis, but their low spatial resolution^[24] (in the range of half millimeter) represents a negative impact in accurate detailed applications. To solve this limitation and to achieve spatial resolutions in the order of micrometers are used optical methods such as conventional and confocal microscopy. Although, these techniques cannot penetrate much deeper under the surface of biological tissues^[24].

And so, it has been proved the need for an imaging modality that is fast and contactless, and mostly fills the need between cellular and full-body modalities by operating in μm and mm scales. Therefore, optical coherence tomography fulfils the previous requirements and allows a whole new world of applications providing better morphological information on, particularly to this study, atherosclerotic plaques^[10]. Figure 2.5 represents a comparison between the mentioned imaging methods.

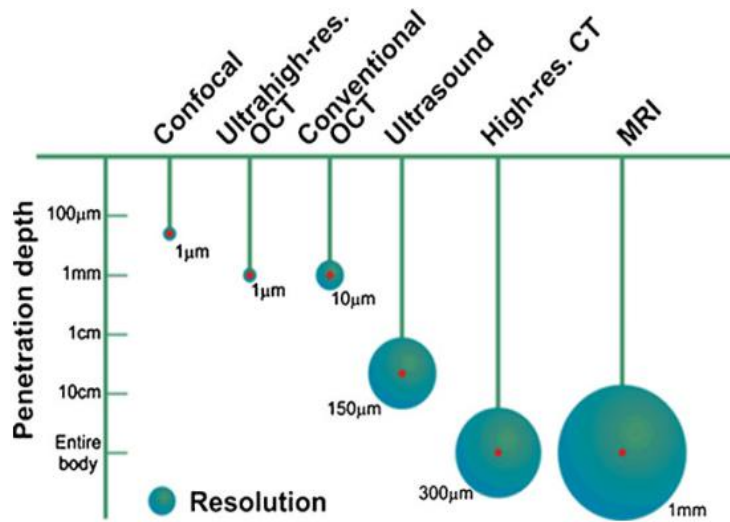


Figure 2.5: Comparison of various imaging methods according to their resolutions and penetration depths

Optical coherence tomography (OCT) is an intravascular imaging technique that processes backscattering light in a range of wavelengths absorbed by biological tissues. More particularly, the processing of backscattered near-infrared light (1280 to 1350 nm)^{[25][7]} allows the acquisition of high-resolution cross-sectional^[7] tomographic images of inhomogeneous and highly scattering samples, like biological tissues^[26].

Also, OCT's physical principles are analogous to ultrasound imaging with respect to wave mechanics but instead of sound uses light, more particularly, low coherence and interferometry phenomena^[27]. In order to understand OCT's acquisition mode, it is important to understand the operation mode of a Michelson interferometer^[26] (Figure 2.6) since their basic setup is similar.

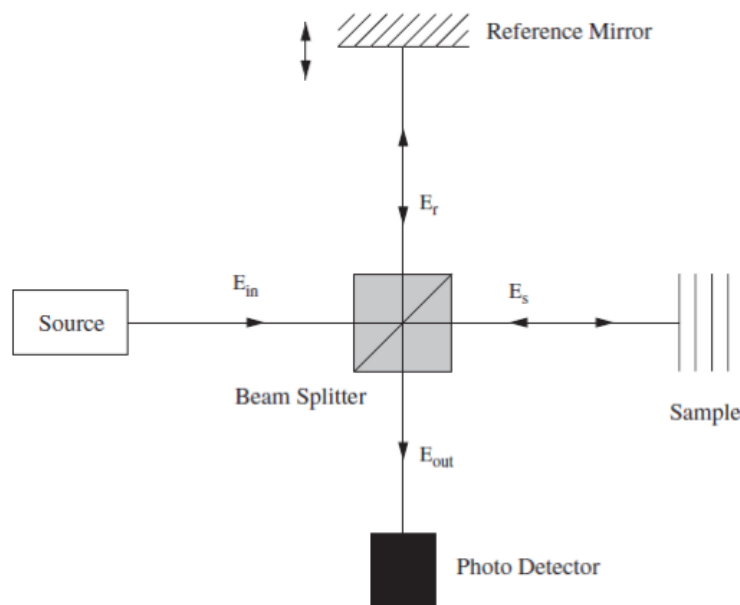


Figure 2.6: Michelson's interferometer basic setup

The light source emits a beam with a near-infrared wavelength (λ infrared range between 700nm and 5000nm) that the beam splitter divides into two paths: the reference (E_r) and the sample path (E_s). The reference beam travels a path and is reflected by a moving mirror[26], whereas the sample beam is reflected by the multiple layers of the sample[26]. After driving their proper paths, both beams return to the beam splitter where the reflected beams are recombined (E_{out}). The photodetector obtains an interference pattern, only observed when both optical path lengths (reference and sample) match the coherence length of the light[26]. The interference pattern allows the identification of intensity peaks due to sharp variations in the refractive index between the several layers of the sample[26] and consequently, the structure of the sample itself.

The axial resolution (penetration depth) of an OCT equipment up to 10 μm is determined by the spatial coherence of the light source[26], which provides the information on how monochromatic the source is, whereas the lateral resolution is located in a range of 20 to 40 μm , depending on the optical elements used in the equipment.

Intravascular OCT (IV-OCT) is widely used in the clinical environment to guide procedures providing anatomical information during trans-catheter coronary interventions (atherectomies and stent placements). OCT imaging alone can provide morphological information^[9] but does not directly provide molecular specific information, as so it is necessary the use of contrast agents with specific biomolecular targets^[10]. A clinical OCT system operates with a 1350 nm swept-source laser, coupled with a single-mode fiber (SMF) which is incorporated into a catheter^[10]. The catheter's diameter commercially used is 0.9mm^[19]. For further information on optical coherence tomography principles please search reference [24].

It is possible to establish a comparison with other intravascular imaging techniques, in order to explore OCT's advantages. Although coronary angiography is the golden standard for guided procedures^[7] it has a major drawback of not being able to evaluate and quantify intracoronary thrombus. However, OCT is able to detect and characterize coronary thrombosis with great accuracy and sensitivity (around 100%). Also, OCT shows greater sensitivity in diagnosis plaque rupture^[7] (about 73%) than angiography (about 47%) and IVUS (about 40%).

2.6 Antibody – Properties and functions

Antibodies are proteins carried by plasma cells and produced by the immune system when an unknown substance (antigen) is detected. After being produced, antibodies are released and bind to specific antigens, which are expressed by different types of cells. The five classes (IgM,

IgD, IgG, IgA, and IgE) of antibodies have the same basic structure^[28], as presented in the figure 2.7, resulting in a Y shaped molecule.

The variable region adapts into various structures according to the differences of the antigens. Particularly, IgG is the most common type of immunoglobulin in human circulation, allowing better control of tissue infection .

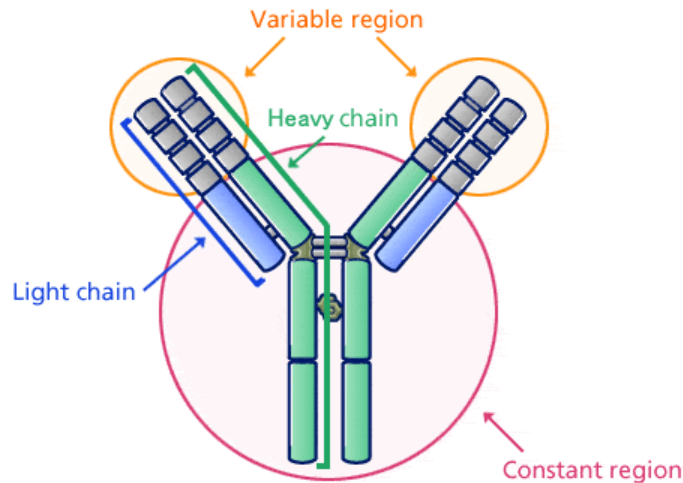


Figure 2.7: Antibody basic structure

Adapted from [28]

2.7 Confocal Microscopy

Confocal microscopy is an imaging tool which generates distinct images of samples which would appear blurry under a conventional microscope^[29], by excluding light that does not belong to the microscope's focal plane. When compared to conventional techniques, confocal microscopy generates less hazed and higher contrasted thin cross-sectional^[29] images.

Currently, and due to the progress in innovative technologies, confocal microscopes are considered completely integrated electronic systems and are composed of the following components^[29] as it is possible to verify in figure 2.8:

- Light source, usually 3 to 5 laser systems to regulate with high precision the beam's wavelength;
- Filters, used to separate multiple light beams based on their wavelengths;
- Acoustic optical deflectors (AOD), used to increase scanning time of images per second (from 3 times per second to 30 times per second on 512x512 pixels images);
- Scanner, to collect the sequential beams of light passing through the sample (stage scanning and beam scanning);

- Spectral detector (PMT, APD), used to identify with high resolution fluorophores spectrum (example: Alexa Fluor488, Alexa Fluor532, Alexa Fluor546 or DAPI);
- Spatial pinhole, used to eliminate out-of-focus light on samples thicker than the focal plane.

In this microscopic technique the image is generated by scanning multiple collimated light beams focused by an objective lens and detected by a photomultiplier through a pin hole. The sequence of points of light is then converted to an image and displayed by a computer. Since the microscope only has one focal plane at a time, it is never possible to have a complete image of the sample^[29], so in each instant only one point of the sample is analyzed.

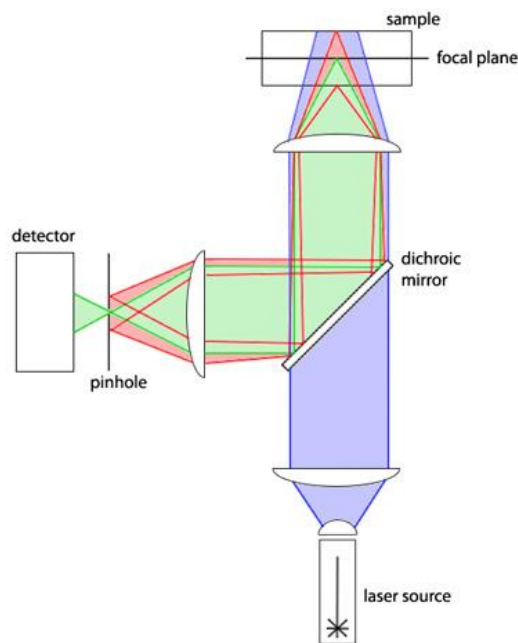


Figure 2.8: Schematic representation of laser scanning confocal microscope
Adapted from [29]

In order to demonstrate the benefits of using this microscopic technique instead of other conventional techniques, table 2.2 presents the advantages and disadvantages of a laser scanning confocal microscope.

Table 2.2: Vantages and disadvantages of laser scanning confocal microscopy

<i>Technique</i>	<i>Advantages</i>	<i>Disadvantages</i>
<i>Laser Scanning confocal microscopy</i>	<p>Ability to scan thin optical sections (0.5 – 1.5 μm);</p> <p>Control depth of field and provide high level of confocality;</p> <p>Isolate and collect a full plane of focus while eliminating the blurry out of focus;</p>	<p>Since the image is acquired point by point it consumes a lot of time to complete one image;</p> <p>The slightest movement can result in image poor definition;</p>

<i>Technique</i>	<i>Advantages</i>	<i>Disadvantages</i>
<i>Laser Scanning confocal microscopy</i>	Reduce background information outside the focal plane; Accurate signal discrimination due to improved z-resolution; Illuminate one single point to avoid undesired scattering; Minimum sample preparation or instrument configuration.	Phenomena of <i>co-localization</i> , meaning the overlap of 2 or more fluorescence emission signals; High level of confocality compromises detectible fluorescence of the sample.

2.8 Atomic Force Microscopy (AFM)

It is notable the recent and most common application of atomic force microscopy to study nanoscale phenomena, with an emphasis on biomedical applications. With this kind of equipment, it has become possible to measure non-conductive samples and its surface topography with a sub-nanometer resolution^[30]. In order to obtain the sample morphology (only at the surface) at an atomic scale, AFM uses a flexible cantilever that goes through the sample's surface to recognize its topography. By monitoring the deflection of the laser beam in the cantilever (detected in the photodiode above the sample), it is possible to measure the force between the tip and the sample. Figure 2.9 represents the general presentation of AFM equipment.

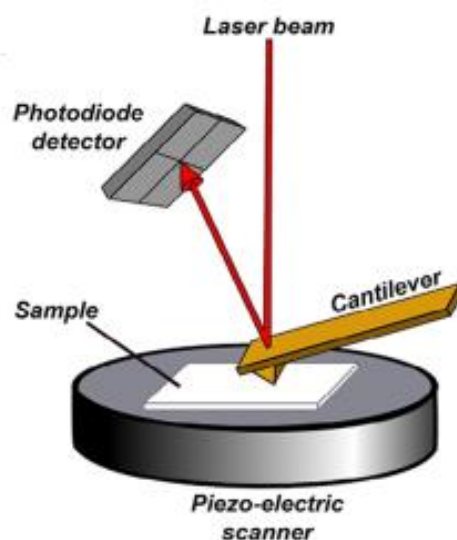


Figure 2.9: Schematic presentation of AFM

Adapted from [30]

During scanning, in order to ensure that the only measured forces are the ones in interest, it is crucial to separate the contributions of the different forces in action and to eliminate the undesired ones.

Since the analyzed samples can have various properties, AFM can be operated in different modes that are exposed in Table 2.3.

Table 2.3: AFM modes

<i>AFM Mode</i>	<i>Operating Mode</i>	<i>Advantage</i>	<i>Disadvantage</i>
Contact	The tip moves across the surface of the sample, and the beam is deflected according to its topographic profile. It can be operated in both <u>constant force</u> and <u>height</u> mode.	In <u>constant force mode</u> , the height movement of the sample results in the surface morphology of the sample. In <u>constant height mode</u> , quicks scans are acquired with small height differences.	The presence of frictional forces can destroy biological samples because the tip of the cantilever is always in touch with the sample's surface.
Non-contact	Using big spring constant cantilevers, it is possible to recognize the surface of the sample in the analysis.	The negligible frictional forces make this method capable of measuring biological samples without damaging its surface.	Low lateral and z resolution of the measurements.
Force modulation	The existence of repulsive forces is used to determine the sample's properties.	High-resolution measures and absence of destruction of the surface's sample.	Difficulty to find the exact distance where repulsive forces act.
Phase imaging	Comparing the phase shift of the cantilever and the driving signal is possible to identify the properties influenced by the interactions with the AFM tip – friction, adhesion, and high elasticity.	Sometimes the unique way to identify differences between local regions of the samples.	

Amplitude modulation	A force gradient is created above the surface of the sample, where the cantilever oscillates and moves through.	Eliminates the major weakness of the non-contact mode related to lack of resolution. It is the most used method in biological applications due to its high resolution and absence of destruction of the surface.	
----------------------	---	---	--

2.9 Scanning Electron Microscopy (SEM)

Scanning electron microscopy (SEM) stands for a technique that uses high energy electron beams instead of light to obtain an image^[31]. The accelerated electrons that compose the beam carry kinetic energy, which is dissipated when the beam reaches the solid sample, producing numerous signals^[32]. Figure 2.10 illustrates a common SEM assembly.

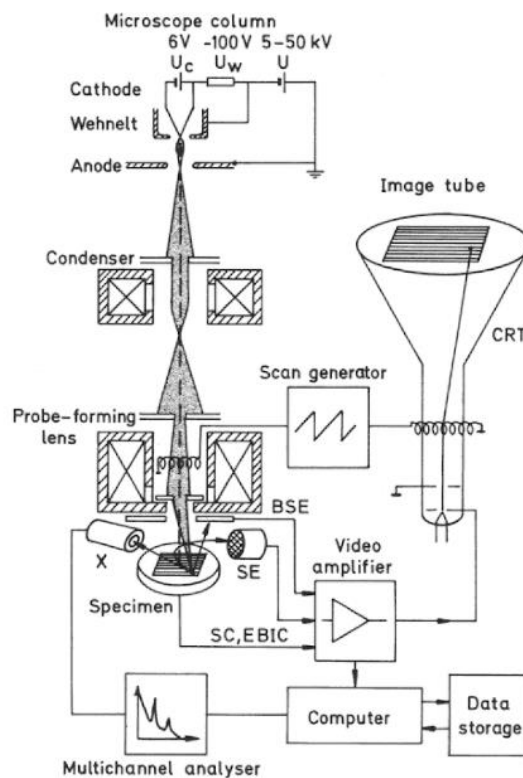


Figure 2.10: Common SEM assembly

Adapted from [31]

According to the figure 2.11 interactions between the electrons and the sample include the production of secondary electrons, backscattered and diffracted electrons and Auger electrons, as well as X-Ray quanta^[31].

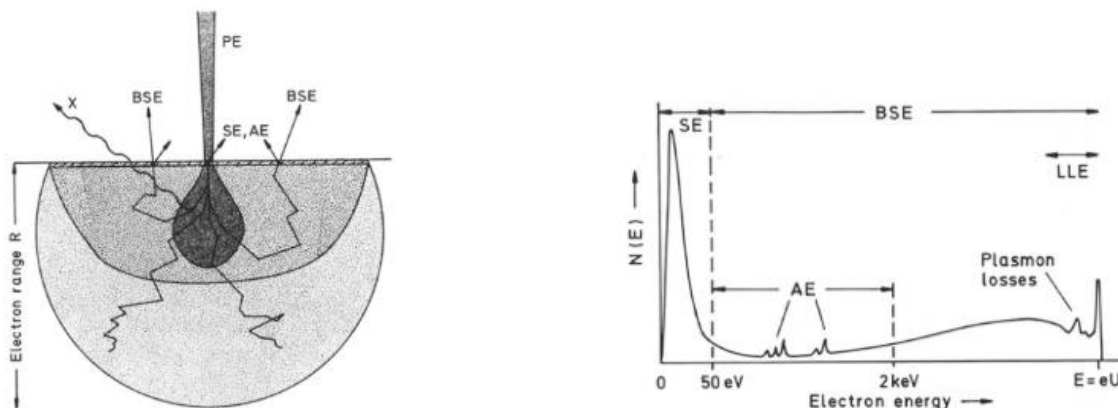


Figure 2.11: SEM interactions

SE – secondary electrons ; BSE – backscattered electrons ; AE – Auger electrons ; X – photons (X-Ray);
PE – primary electrons (initial beam)

Adapted from [31]

The interactions between the electrons and the sample generate signals at the surface of the sample that allows the identification of several parameters:

- Surface's texture (morphology and topography) due to the signal provided by the secondary electrons;
- Chemical composition due to the elemental analysis provided by the photons (X-Ray);
- Crystalline structure due to the signal provided by the diffracted electrons;
- The orientation of the materials in the surface due to the signal provided by the backscattered electrons.

In the table presented below (Table 2.4) are discussed the advantages and disadvantages of this microscopic technique.

Table 2.4: Advantages and disadvantages of SEM technique

<i>Advantages</i>	<p>Possibility to characterize solid materials</p> <p>Higher control in the degree of magnification due to the use of electromagnets (instead of lenses)</p> <p>Minimal sample preparation and large depth of field</p> <p>High speed in data acquisition (mostly less than 5 minutes)</p>
<i>Disadvantages</i>	<p>Radiation (X-Ray) is produced during the process</p> <p>Samples must be solid and small enough to fit in the chamber</p> <p>Stability in the vacuum must be guaranteed</p> <p>Impossibility to detect elements with an atomic number under 11</p>

3. Experimental Methods

3.1 Tissue Simulator Phantom Design

Phantoms are artificial structures (physical or computational) used to replicate certain conditions or behaviors of the human body. In this scope, phantoms were developed to reproduce optical properties^[33] of a range of tissues present in human arteries.

Previously, phantoms were made of hydrogel and resin but entailed disadvantages^[33] like short durability and impossibility to form complex configurations (in the case of hydrogel) or higher stiffness than soft tissue (in the case of resin).

Alternatively, silicone, fibrin, and PVA-C (poly (vinyl alcohol) cryogel) represent the most promising materials^[33] to reproduce tissues properties in OCT imaging. The two most critical optical properties to analyze in OCT imaging are backscattering and absorption. The chosen material to produce the phantom was silicone, with a mixture of polydimethylsiloxane (PDMS).

PDMS phantoms are relatively easy to produce and have the leading advantage of being adjustable to various purposes:

- The phantom's optical properties can be customized by incorporating scattering agents like titanium dioxide (TiO_2);
- The phantom's mechanical/elastic properties allow it to be shaped into the required format for analysis.

As well as the advantages presented previously, PDMS high toughness and low viscosity before curing represent important characteristics for its ready compatibility with, for example, scattering agents^[33].

The primary difficulty in this process is to obtain a homogeneous distribution of the polymer in the chosen mold without aggregates or air bubbles. As so, to overcome this obstacle, three processes were applied to the phantom: sonication of the mixture to avoid aggregates, degassing under vacuum to remove air bubbles and, after curing, thinning the silicone with hexane to remove impurities from the surface.

The following components compose each silicone kit and the phantom is combined in the ratio of 10:1^[20]:

- A compound – PDMS Sylgard 184 silicone elastomer kit;
- A catalyst – curing agent.

In order to accelerate curing, the samples were heated at 65°C for 1 hour and 30 minutes.

As so in order to replicate tissue's behavior to NIF light, multiple versions of the phantom were developed, as it is possible to verify in figure 3.1:

- One layer 2 mm thickness of PDMS
- One layer 2 mm thickness of PDMS incorporated with TiO₂ (0.5% , 1% and 2%)
- Double layer 2 mm thickness of PDMS incorporated TiO₂ (0.6% and 3%)



Figure 3.1: Developed phantoms - (a) one-layer clear PDMS (b) one-layer PDMS incorporated with TiO₂

The double layer phantom was shaped to replicate the different layers that constitute human arteries and it was taken in consideration the different scattering each one produces. A schematic is presented in figure 3.2 with the 2 steps of phantom shaping.



Figure 3.2: Schematic of double layer phantom shaping and the two replicated layers

3.2 Titanium Dioxide Synthesis (TiO₂)

Titanium dioxide (TiO₂) is an inorganic scatterer[33] which can be integrated into silicone-based phantoms. TiO₂ nanoparticle synthesis was performed on CENIMAT laboratories. A hydrothermal-microwave assisted method was performed on a CEM Discover SP – Microwave Synthesizer. The following procedure was followed:

1. In a 100 mL beaker, 55 mL of H₂O were mixed with 5 mL HNO₃ and 2 mL C₁₂H₂₈O₄Ti (titanium (IV) isopropoxide) and mixed under RT until all reactants were dissolved.
2. 20 mL of the solution was transferred into a 35 mL Pyrex pressure vessel which was then placed in the microwave synthesizer.

The parameters used in the process were the following:

Method Parameters

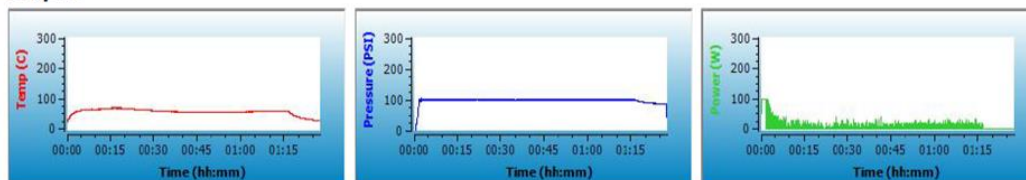
Name: Joxo

Prestirring(mm:ss): 00:00

Type: Dynamic

Stage	Temp(C)	Time(hh:mm:ss)	Pressure(PSI)	Power(W)	PowerMAX	Stirring
1	200	01:15:00	100	100	No	Off

Graphs



3. The resulting material was transferred to falcon tubes and centrifuged to remove supernatant.

4. The powder was then dried at 50°C.

In later phantoms, TiO₂ powder was not synthesized and commercial powders were used due to higher accessibility and lower cost.

3.3 Gold Nanoparticles Synthesis and Immobilization (GNPs)

Citrate stabilized gold nanoparticles used as contrast agents were synthesized using the Turkevich method^[34].

Reagents:

Solvent: DMF

[PVP-10000]= 10 mM

[HAuCl₄]= 0.5 mM

[Au-citrate-PVP]= 1.96655 mM GOLD SEEDS (15 nm diameter but can change with new synthesis)

**Final size with these concentrations should be around 70 nm*

Procedure:

- Dissolve the 2.5 g PVP in the 25 mL DMF and sonicate for 15 min or until it is fully dissolved.
- The stock solution of gold precursor (HAuCl₄) is at 0.1268 M, and since it is needed at 0.5 mM, it will be used a volume of 99.15 μL.
- Under magnetic stirring, add the HAuCl₄ and wait around 2 minutes (the solution gets a bit lighter).

- d) For 25 mL of final solution volume (PVP/DMF/ H₂AuCl₄) at 250 mM, it is necessary 317.82 μ L of 1.96655 mM seeds stock solution (Au-citrate-PVP).
- e) Under magnetic stirring, add the 317.82 μ L gold seeds coated with PVP (Au@Citrate@PVP) and wait for 1h or until full reduction is observed – UV-vis and blueish color.
- f) Perform one washing cycle for 60 min at 5500 rpm and redisperse the solution in isopropanol.
- g) Measure the concentration of the final solution by UV-Vis, Abs₄₀₀.

The absorption spectrum was performed at 400 nm since, at this spectral region, organic molecules and the surface plasmon resonance have only minor influence^[35]. The absorbance is mainly due to interband transitions of gold and therefore can serve as a more robust measure of the gold concentration.

The resulting nanoparticles were then encoded with specific dyes, namely TB (Toluidine blue), NB (Nile blue), MB (Methylene blue) and 1NAT (1 – naphthalenethiol). To the 1NAT dye, 0.8mL of gold nanostar solution was mixed with 2.6667 μ L of MUA, 4.25 μ L of NH₄OH 29%, 10 μ L of 1NAT and IPA until reaching 1 mL of final solution. To the remaining 3 dyes (TB, NB and MB) the same volumes of gold nanostar solution, MUA and NH₄OH 29% were used, only varying the volume of dye – 100 μ L. After continuous magnetic stirring for 2 hours, each of the solutions passed through 2 washing cycles composed by: an ultrasound bath for 2 minutes, centrifuge at 4000 rpm for 30 minutes, remove supernatant and centrifuge at 4000 rpm for 60 minutes. The solutions before and after magnetic stirring are shown in figure 3.3.

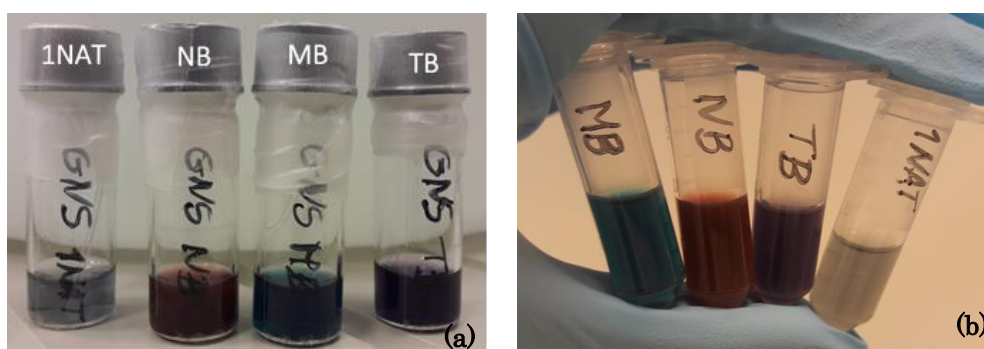


Figure 3.3: Solutions before (a) and after (b) magnetic stirring

The resultant gold nanostars were characterized using a FEI Quanta 650 FEG Electron microscope and absorbance measurements were performed in a Perkin-Elmer LAMBDA 950 UV-VIS-NIR Spectrophotometer.

After activating the PDMS surface with O₂ plasma, effect shown in figure 3.4, a silanization process was performed to attach nanoparticles to the oxidized PDMS. The silane used was γ -APTES (Sigma Aldrich) which has carboxyl-binding active groups on one side and amine

termination on the other one. The PDMS substrates were immersed in several concentrations of ethanol solutions with APTES followed by washing and annealing at 80°C for 1 hour and 30 minutes. Finally, the substrates were immersed into the colloid coded gold nanoparticles solution for 1 hour and 30 minutes and washed with deionized water annealed at 80°C for 1 hour.

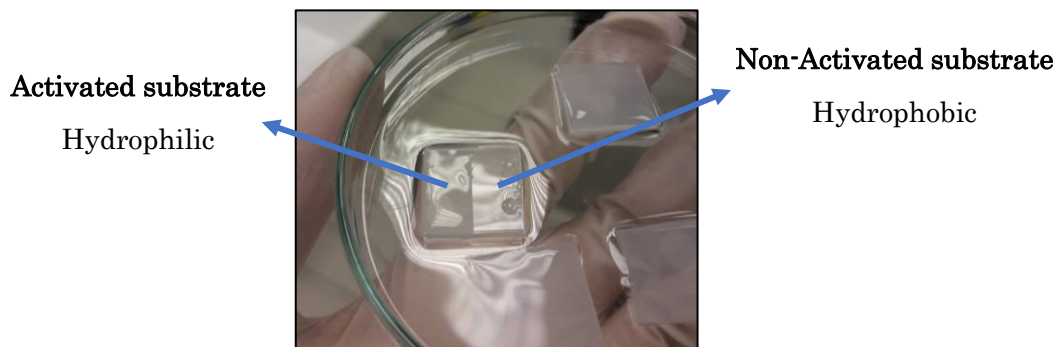


Figure 3.4: PDMS substrates after oxygen plasma activation. Sample with half the surface exposed to oxygen plasma and half covered

At the end of this process it was assured that the gold nanoparticles were attached to the surface of the PDMS through electrostatic forces (schematic shown in figure 3.5).

The characterization of the distribution of the coded gold nanoparticles at the PDMS surface was performed on a Zeiss LSM 780 Confocal Microscope.

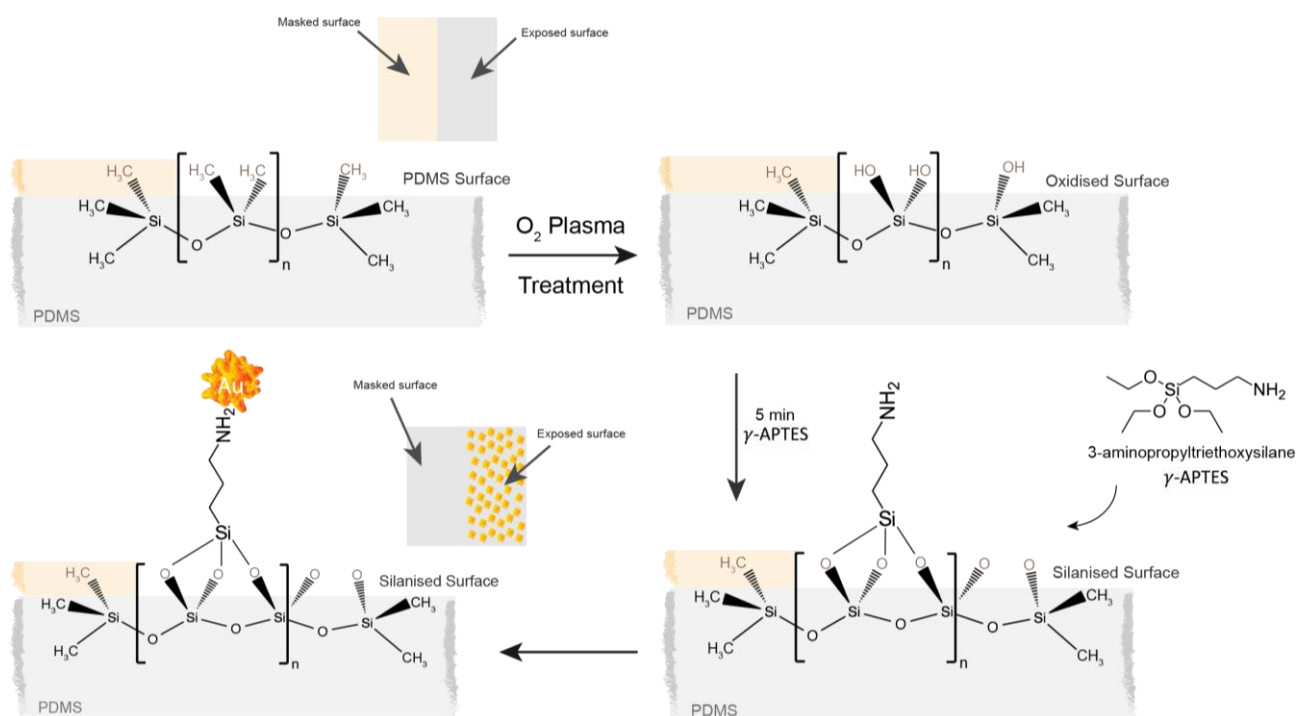


Figure 3.5: Schematic of gold nanoparticles immobilization into the PDMS

3.4 Microbubbles Synthesis

PBCA (poly (n-butyl cyanoacrylate)) microbubbles were not synthesized at INL facilities but were kindly provided by Prof. Twan Lammers (ExMI, Helmholtz Institute for Biomedical Engineering, Germany) investigation group. Figure 3.6 shows the target ready batch received and the schematic illustrates the microbubbles function.

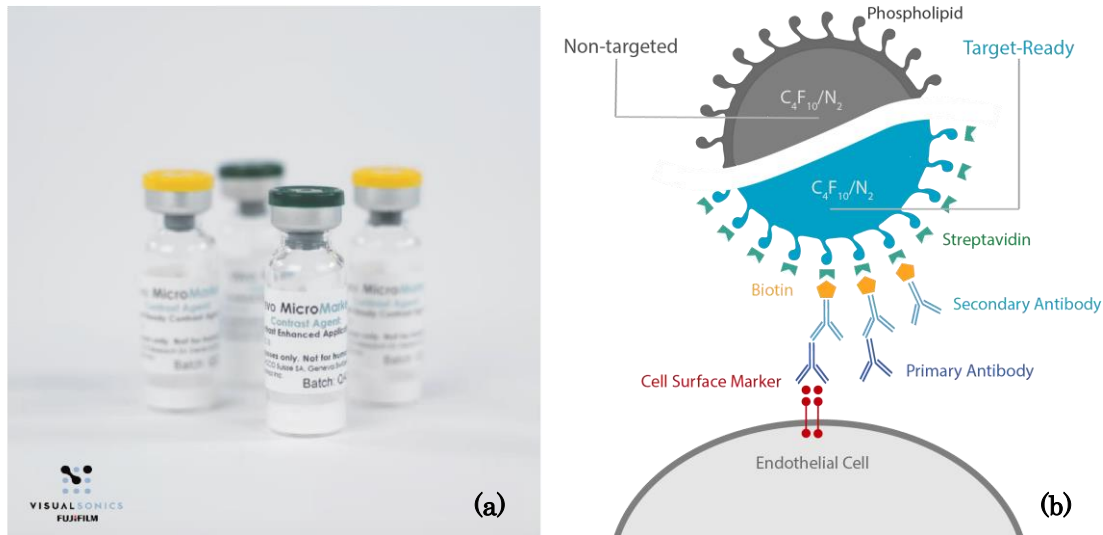


Figure 3.6: Lyophilized VeVo Micromarker stored in a glass vial (a) Schematic representation of non-targeted and target-ready surface modified microbubbles (b)

Initially, the first batch of PBCA[21] microbubbles were received in Triton-X without any surface-active groups and varied in a size range of 1.8 to 2.5 μm diameter. The second batch consisted of Vevo MicroMarker® Target-Ready Contrast Agent (from Fujifilm Visualsonics) produced by Bracco Research SA. Vevo marker agents are lyophilized microbubbles with a lipid-based outer shell containing polyethylene glycol, phospholipids and fatty acids, used to enhance tissue and vascular imaging. Since the microbubbles are lyophilized it is needed to reconstitute them with saline (0.7 mL of solution).

3.5 Functionalization Methods

In order to the microbubble to be recognized by the secondary antibody a biotinalization step was performed on unconjugated goat anti-rabbit IgG (Novex by Life Technologies™, Lot. 62-10-092817) with a biotin labelling kit (Thermo Scientific™ EZ-Link™ Sufo-NHS-LC-Biotin, Molecular Weight: 556.59, Lot. Number A39257 21335). The followed protocol was provided by the user's guide (MAN0016133, Pub. Part. Nr. 21611855).

Initially, a 10 mM biotin solution was prepared with ultra-pure water. Then, an antibody solution was prepared by adding 250µg of antibody stock solution (2.5mg/mL) and 3.65mL of saline. 10µL of biotin solution (initially prepared – 10mM) were then added to the antibody solution and incubated for 1 hour at 4°C. The process is completed after filtering the incubated solution with an 100k Amicon Ultra-0.5 Centrifugal Filter Unit.

From now on secondary antibodies are prepared to bond with streptavidin present in the microbubbles surface.

3.6 Immunohistochemistry

In order to recognize endothelial cells, primary antibodies (rabbit anti-VE-cadherin - Thermo Fisher, code: V1514-200UL, Lot. 016M4804V) passed through the first step of immunohistochemistry process.

As so, a PBS solution containing 1% of bovine serum albumin (BSA) was prepared. To 4mL of the prepared solution were added 20.4µL of rabbit anti-VE-cadherin (primary antibody). The positive sample was submerged in the solution containing primary antibodies while the negative sample was submerged in a PBS blocking solution with 3% BSA. Both samples were left incubating overnight (8 hours) at 4°C. After, the samples were washed 3 times and placed in a PBS solution. According to the user's guide, further microbubble functionalization was performed.

Using a syringe, 0.3mL of the filtered biotin-labeled antibodies solution were drawn and injected into the microbubble vial (already prepared), followed by gentle agitation for 1 minute. The solution was left to rest at room temperature for 15 minutes. From now on, the microbubbles are fully assembled and ready to use.

Thus, the second step on the immunohistochemistry process was performed by transferring the target-ready microbubbles solution into the positive artery vial. The solution was left to incubate while agitating for 1 hour at 4°C, followed by 3 washing cycles in PBS.

4. Phantom Characterization Methods

Multiple characterization methods (confocal microscopy, scanning and transmission electron microscopy and atomic force microscopy) were applied in order to assure the physical properties of the synthesized contrast agents (gold nanoparticles and microbubbles) and scatters (titanium dioxide) as well as the immobilization and functionalization of the phantoms with the already referred contrast agents.

4.1 Confocal Microscopy

At INL facilities, a Zeiss LSM 780 Confocal Microscope, was used to:

- a) visualize with detail different dilutions (stock, 1:4 and 1:40) of the original stock solution of microbubbles, as presented in figure 4.1;

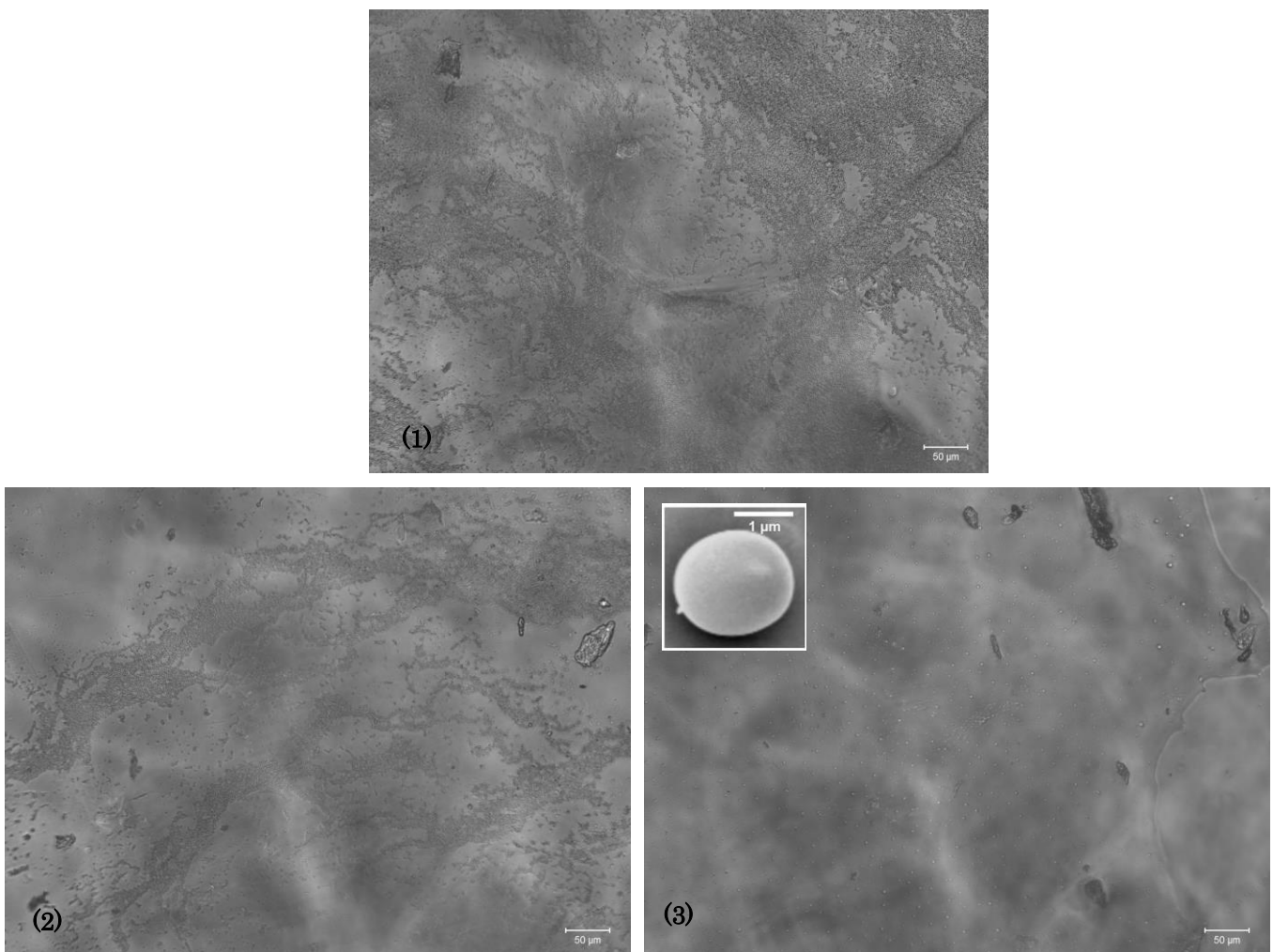


Figure 4.1: Microbubbles confocal images (1) stock solution (2) 1:4 dilution (3) 1:40 dilution

- b) visualize the border of a drop of a microbubble's solution in a blade, as shown in figure 4.2;

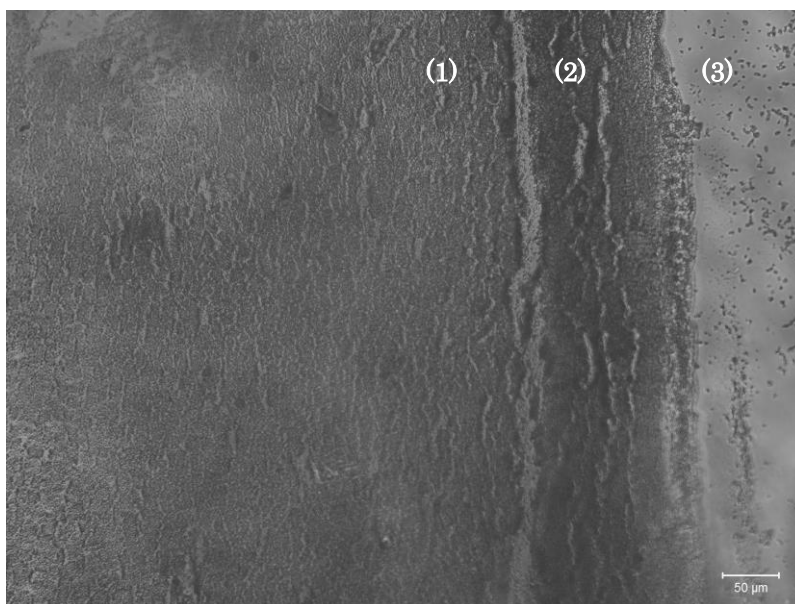


Figure 4.2: Dried drop of microbubbles' solution showing a clear aggregation of microbubbles on the edge (2) forming an interface between the interior of the drop (1) and the blade itself (3)

- c) assure the existence of an interface between the functionalized and non-functionalized part of the phantom containing immobilized gold nanoparticles, as shown in figure 4.3. Using a laser with a wavelength of 633nm, a fluorescence process occurs in the Nile blue dye present at the surface of gold nanoparticles emitting a signal at 660 nm, visible as red dots in the image.

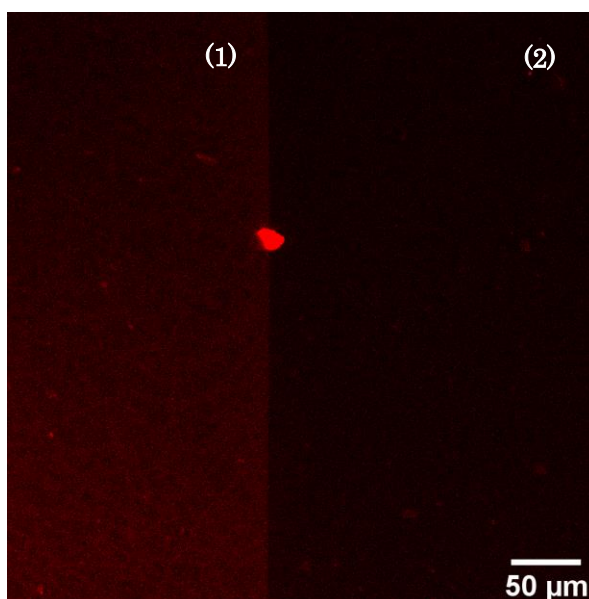


Figure 4.3: Interface created showing the difference between functionalization (1) and non-functionalization (2) in the immobilization of gold nanoparticles in the phantom

4.2 Scanning and Transmission Electron Microscopy (SEM and TEM)

At INL facilities, a Fey Quanta 650 FEG Scanning Electron Microscope was used to:

- a) visualize the differences between laboratory synthesized titanium dioxide (protocol mentioned above) and commercial titanium dioxide, as shown in figure 4.4;

It was chosen to use the commercial titanium dioxide due to the lower cost, higher quantity available and no need for particle uniformity.

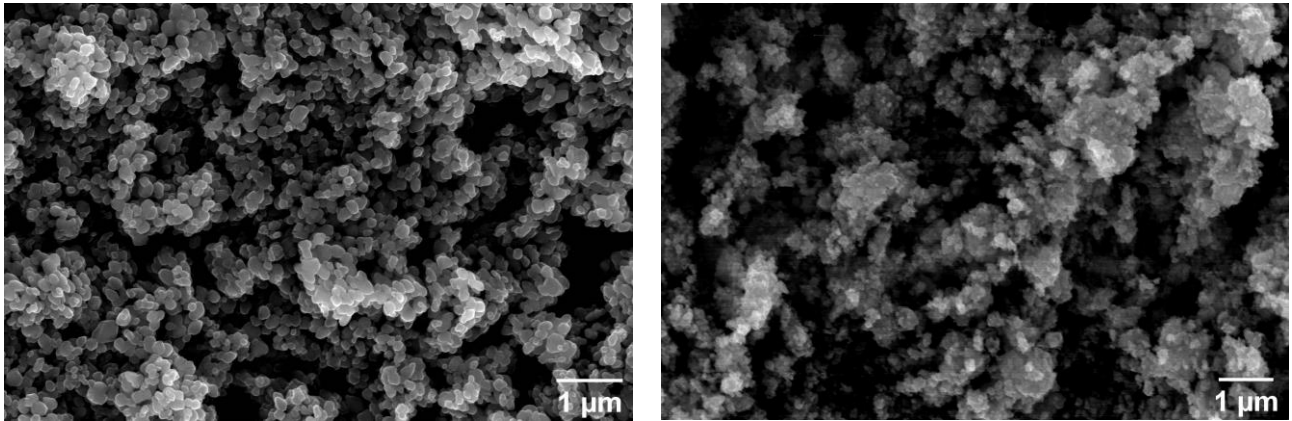


Figure 4.4: SEM images of titanium dioxide acquired commercially (left) and synthesized (right)

- b) ensure the star shape of synthesized gold nanoparticles with the protocol mentioned above, as presented in figure 4.5.

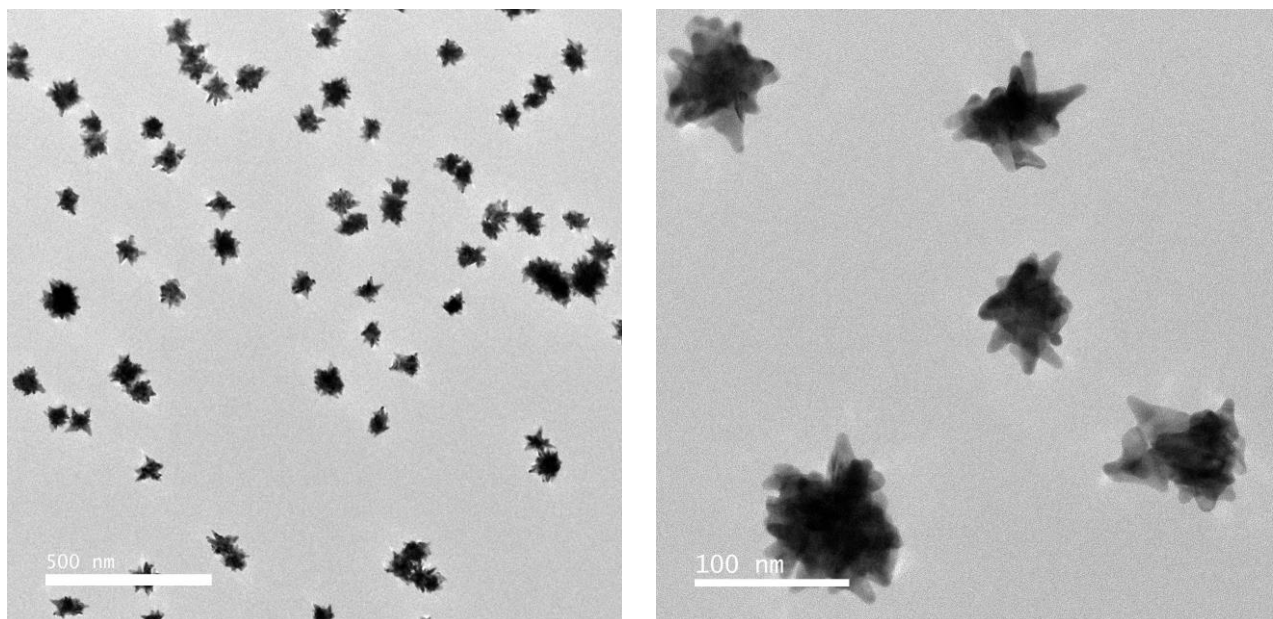


Figure 4.5: TEM images of synthesized star-shaped gold nanoparticles

Posteriorly was performed a size distribution of the star-shaped synthesized gold nanoparticles, batch named MC01 in the histogram presented in figure 4.6, leading to an average particle diameter of 55 nm. Considering that the nanostars have an amorphous shape, they will probably have a much higher diameter from one end to the other, but the average diameter provided by the histogram is particularly useful to calculate the average volume of the particles.

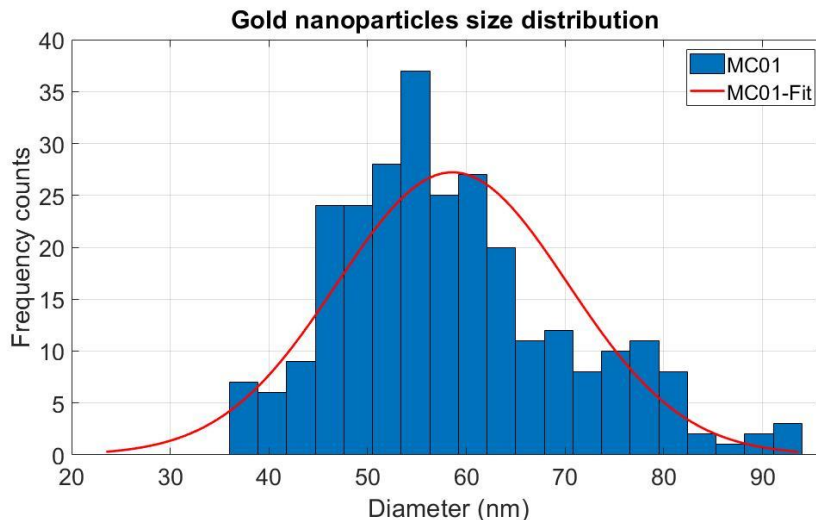


Figure 4.6: Histogram presenting gold nanoparticles size distribution

4.3 Atomic Force Microscopy (AFM)

At Cenimat facilities (Faculty of Science and Technology – NOVA University), an atomic force microscope was used to assure the immobilization of gold nanoparticles at the surface of the PDMS phantoms. Although an increased roughness was verified at the surface of the phantom, as presented in figure 4.7, comparatively to the surface of the clear phantom, it was impossible to assure the nanoparticles were immobilized.

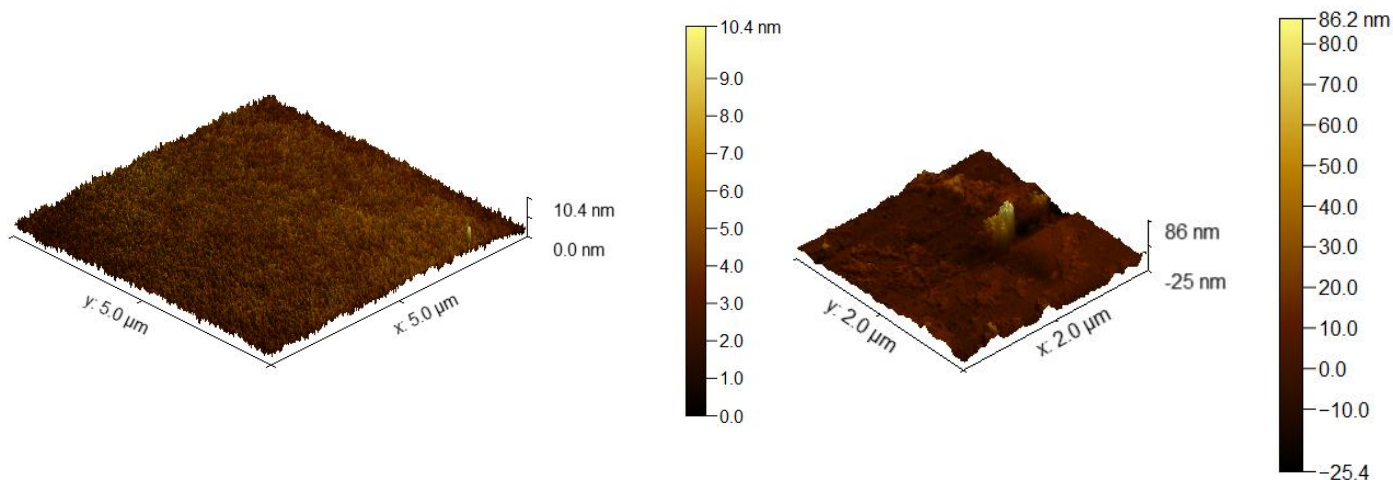


Figure 4.7: AFM roughness measurements comparing clear PDMS (maximum 10.4 nm surface) and PDMS with gold nanoparticle at the surface (maximum 86 nm detected)

5. Image Acquisition

5.1 Acquisition Methods

To perform optical coherence measurements were used at Vigo's Hospital a Lunawave Coronary Imaging Consola with Fast view coronary catheter (Terumo Corporation™, ASHITAKA, Japan) and at Hospital de Braga a ILUMEN FD-OCT System from ABBOTT (formally Saint Jude Medical, St. Paul, MN) with a c7 dragonfly catheter.

Firstly, were performed at Hospital de Braga, measurements with one layered phantoms, according to the assembly presented below, as well as calibration measurements. The original assembly used microtubes to contain the phantom adhered to its inner walls. So, as illustrated in figure 5.1, the first step of the assembly was the preparation of the sample (A) followed by the necessary arrangement of the phantom to fit in the tube (B). Finally, the phantom is placed inside the Eppendorf tube to fit its inner walls (C). Note that, in case of calibration were used empty Eppendorf tubes so step A and B were not performed.

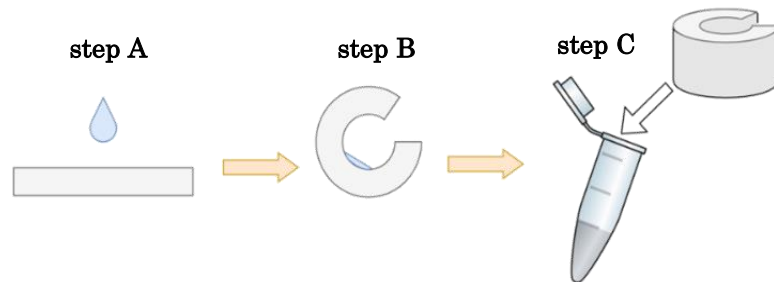


Figure 5.1: Original sample preparation to perform OCT measurements

Also, a photograph taken in Hospital de Braga, at the same time a measurement was performed, is presented in figure 5.2 to visualize the sample assembly with the optic fiber of the OCT equipment.

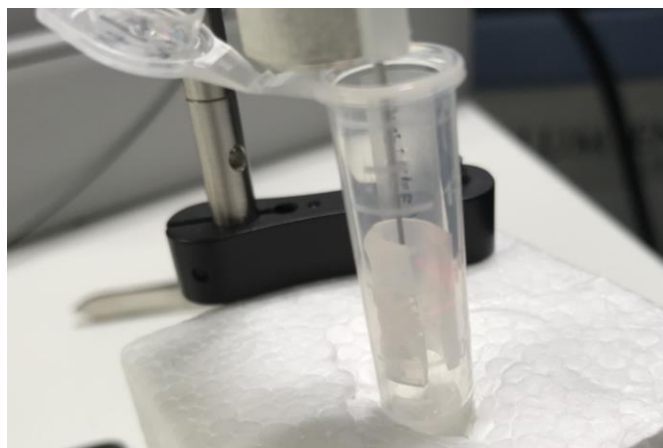


Figure 5.2: Complete assembly of an OCT measurement

Posteriorly, it was adopted a new assembly, presented in figure 5.3, to perform the OCT measurements in arteries (Vigo's Hospital) and in double layered phantoms (Hospital de Braga). Instead of an Eppendorf's tube was used a larger plastic tube and it was assured an immobilization of the optic fiber.

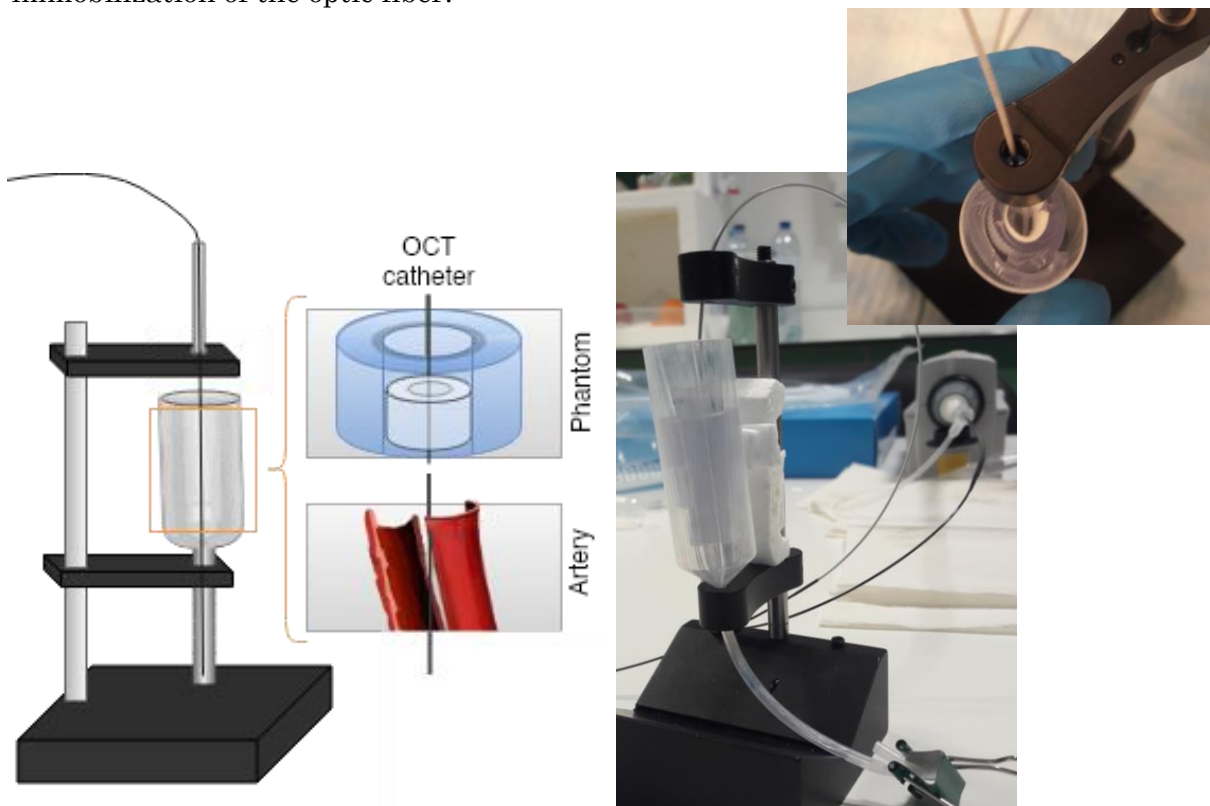


Figure 5.3: Final OCT measurement assembly (left) schematic including arteries and phantoms (right) photograph taken in the moment of an OCT measurement in Hospital de Braga, with a upper vision of the complete assembly with a phantom

Figure 5.4 represents a schematic of the order in which an OCT measurement is performed and how the image is obtained.

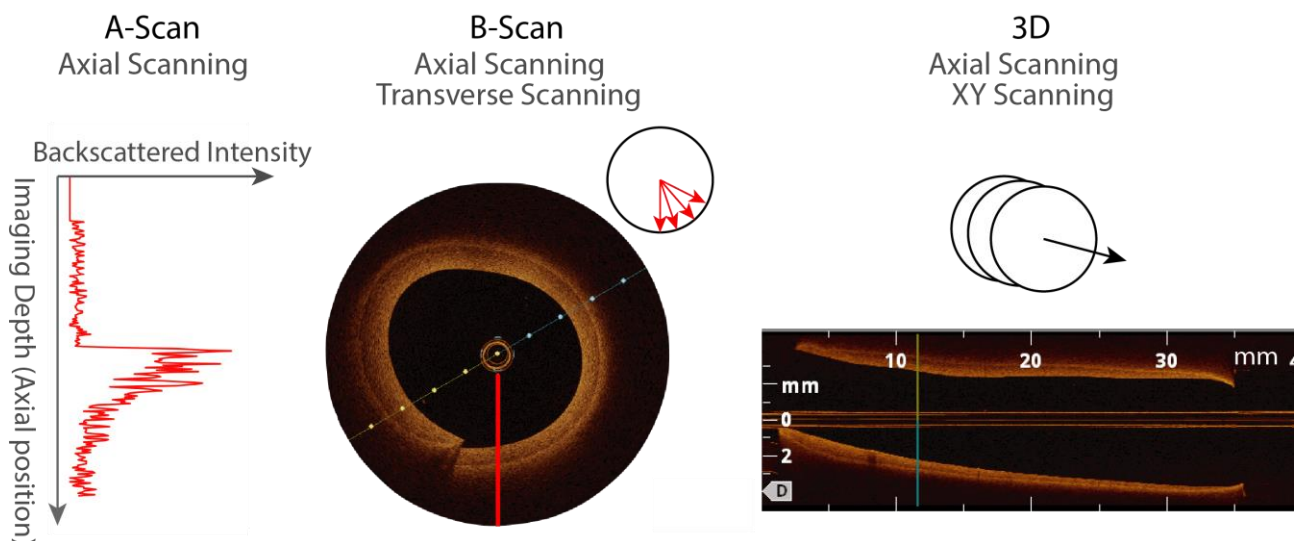


Figure 5.4: Schematic of OCT imaging acquisition mode

Firstly, a map of the reflectivity of the sample along an axial depth direction is obtained composing an A-scan. In the obtained image, an A-scan represents one radial line. Then, through the combination of a series of axial depth scans (A-scan), are obtained the cross-sectional scans of the sample, composing the B-scan. The final image is a composition of a series of radial lines. Three dimensional (3D) reconstructions are obtained by scanning series of B-scans.

In the case of the phantom's measurements, calibration procedures of the OCT equipment were performed with an empty Eppendorf tube to measure the air response to NIR light and with an Eppendorf tube filled with deionized water. The obtained images after calibration are presented in image 5.5. For further reference, the optical fiber always remains at the center of the image (independently of the equipment used).

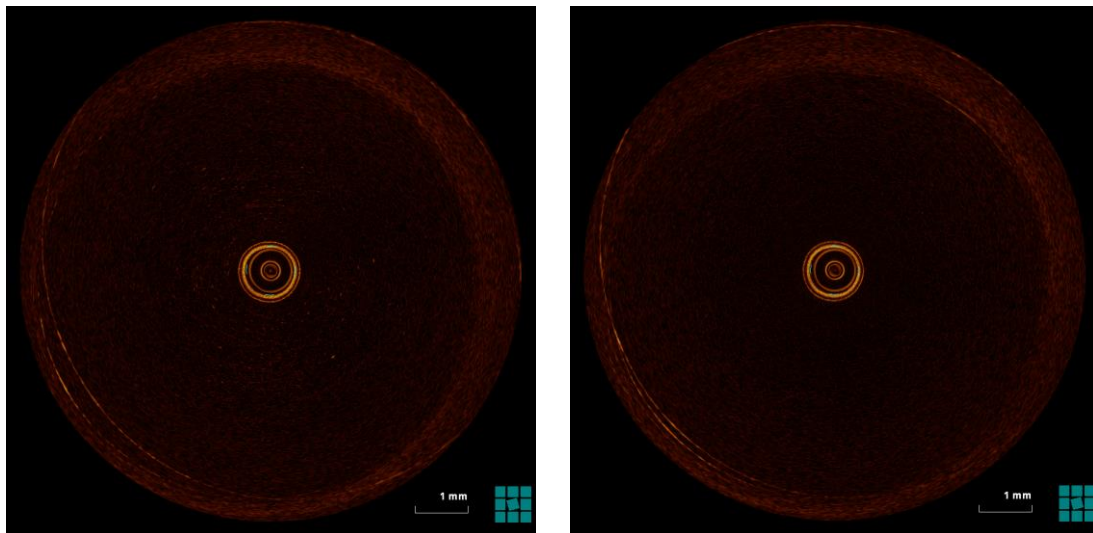


Figure 5.5: Calibration procedures with deionized water (left) and air (right)

Relatively to the measurements with post-mortem arteries, calibration procedures of the OCT equipment were also performed with air and water but additionally with PBS (Phosphate-buffered saline) since its solution preserved the viability of the arteries.

As mentioned before, titanium dioxide (TiO_2) was used as a light scatterer to replicate biological tissue behavior to NIR light. According to Figure 5.6, the increased brightness compared to the clear PDMS assures the titanium dioxide elevated scattering of light in a PDMS medium.

Besides calibration procedures were also performed individual measurements of the phantoms or arteries without the contrast agent to establish negative (without contrast agent) and positive (with contrast agent) controls. Figure 5.6 represents negative controls performed at Hospital de Braga with OCT measurements of clear PDMS, one-layer phantom of PDMS and TiO_2 , double-layer phantom of PDMS and TiO_2 .

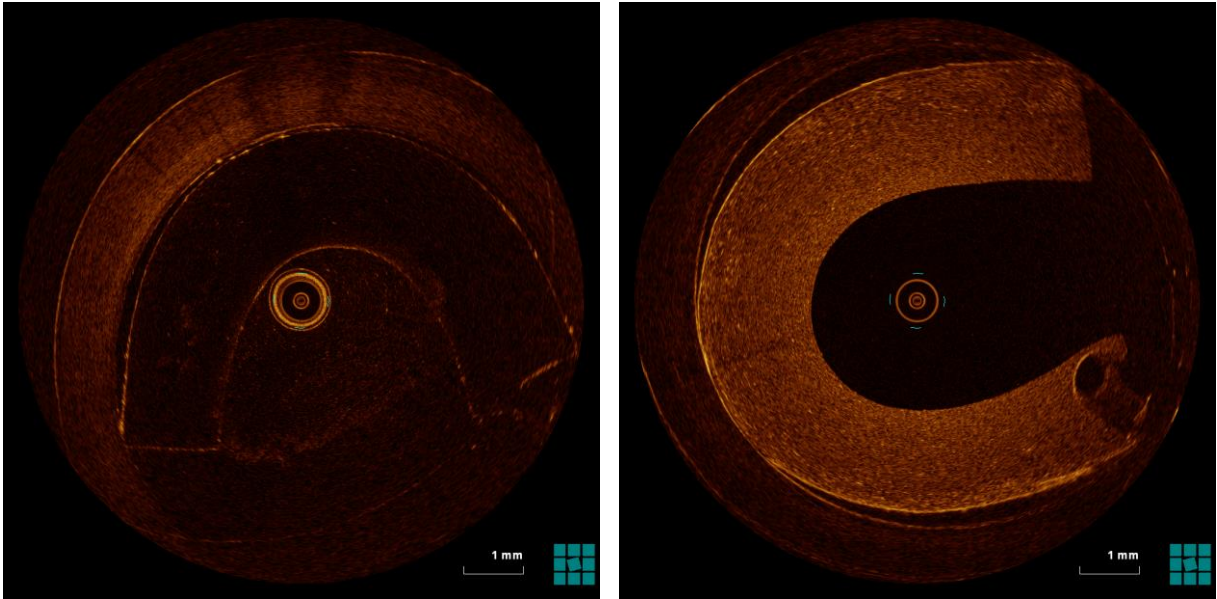


Figure 5.6: OCT measurements of negative controls with clear PDMS (left) and one-layer phantom of PDMS and TiO₂ (right)

5.2 Processing Tools

After calibration procedures and negative control measurements, were acquired images in order to evaluate which of the synthesized contrast agents (gold nanoparticles and microbubbles) provided the best contrast enhancement in OCT measurements.

The comparison between the obtained images are presented in figure 5.7 and it is clear a considerable difference between the signal provided by the gold nanoparticles and the microbubbles.

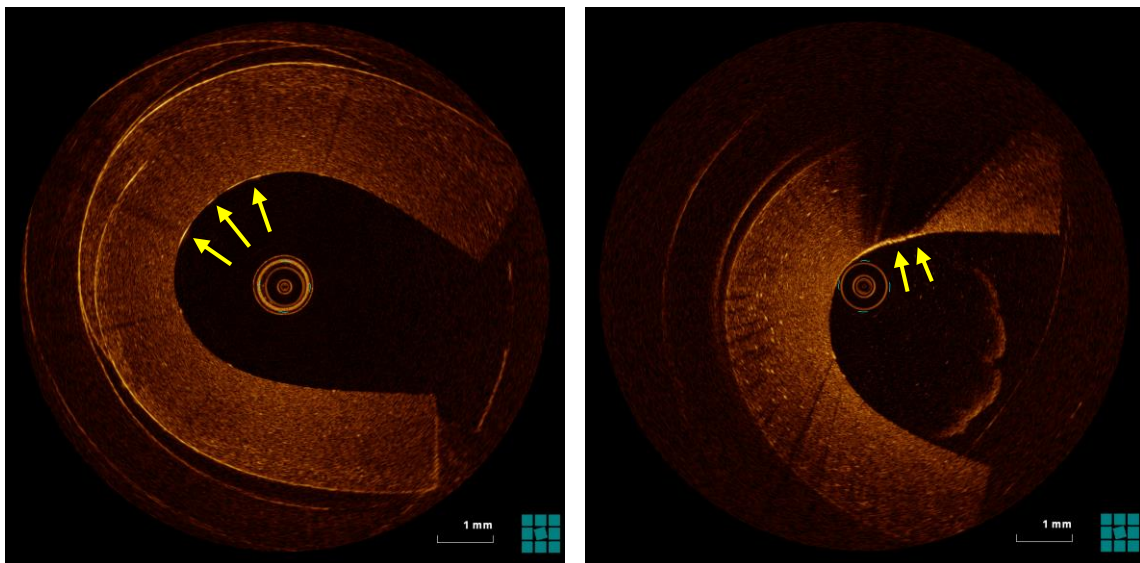


Figure 5.7: Comparison between the provided signal of gold nanoparticles (left) and microbubbles (right). The yellow arrows show the exact location of the contrast agent

Not only microbubbles are larger in diameter than gold nanoparticles (1.2 μ m to 60nm) but also provide better signal in OCT images, increased brightness and more pronounced shadow. Also, microbubbles present less side biological effects, as analyzed in chapters 1 and 2, proving to be the best contrast agent. Further analysis and all the measures presented after will consider microbubbles as the contrast agent. Gold nanoparticles were no longer analyzed after the discovery of a better contrast enhancer.

After concluding which of the contrast agents would be used to further acquisitions and finishing OCT measurements in different conditions (phantoms and human arteries), was developed an algorithm to automatically detect the regions where the microbubbles were located. It is important to reinforce that by detecting with precision the location of the microbubbles, the algorithm is providing the location of a possible unstable lesion when, in the future, is used in real time procedures. The software used to develop the algorithm was Matlab version 2019.

As mentioned in chapter 2.5, the basic principle of optical coherence tomography is the analysis of backscattered light. If the material is highly scattering, the OCT image will appear very bright because when light is emitted in every direction, the material allows the beam to get through it. Contrarily, if the analyzed material is a low scatterer, the OCT image will appear darker, because the material retains the light in a single point (highly bright) and blocks its spreading.

Keeping these differences in mind, is possible to analyze figure 5.8 and clearly notice the difference between a high scattering medium (marked as I in the image), titanium dioxide, and a low scattering material (marked as II in the image), microbubbles. It also becomes possible to visualize that the contrast agent (microbubbles) retains light, producing a very bright region followed by a shadow.

As so the developed algorithm, in order to detect the location of the contrast agent, localizes the regions that present increased brightness (higher intensity) followed by a shadow through its profile of intensity. Regions of interest (with shadow) will present a very well-defined peak of intensity and remaining signal with low intensity. Contrarily, regions without a shadow will present several consecutive less intense peaks and a remaining signal with low intensity. Further will be explained how the algorithm evaluates if these 2 conditions were fulfilled.

Besides that, the analysis of the OCT images performed currently by physicians is purely visual and not confirmed by any type of software. As so, it is important to provide an algorithm that confirms the visual analysis previously done but also a complete tool to improve physician's diagnosis to patients.

Figure 5.8 presents, both in a phantom and in a human artery, the regions of interest the algorithm aims to detect.

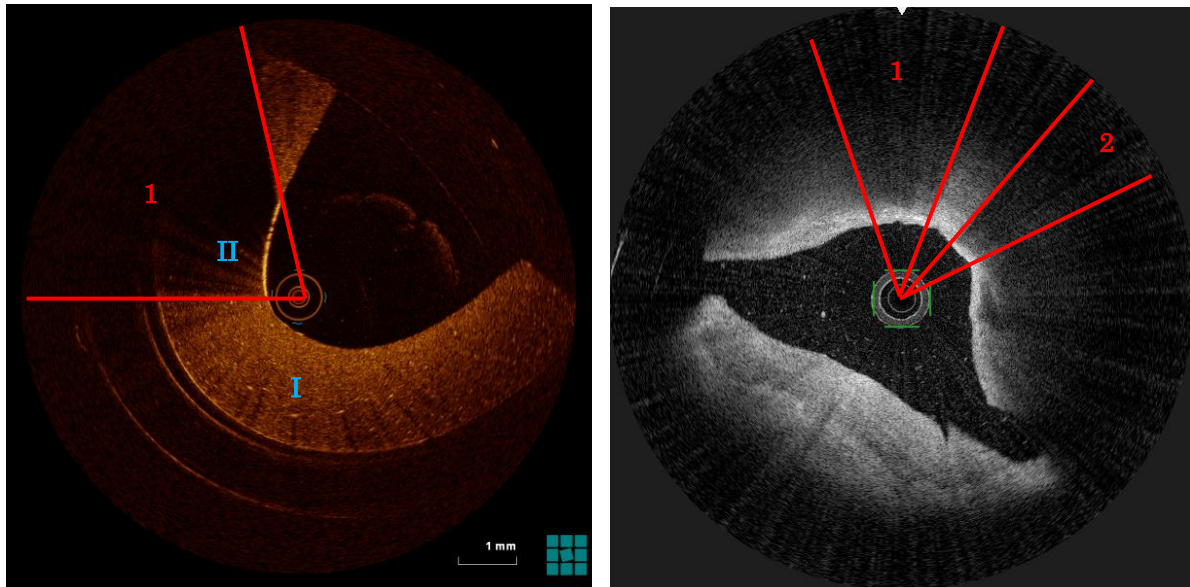


Figure 5.8: Identification of the regions of interest both in and phantom (left – region 1) and in a human artery (right – regions 1 and 2). The red lines establish the boundaries of each region.

Consequently, and as presented in Figures 5.7 and 5.8, the two main characteristics in the OCT signal provided by the microbubbles are increased brightness in a specific spot and pronounced shadow (behind the area, meaning in the opposite direction of the fiber). Since there are two characteristics to be analyzed, the algorithm will be divided in two main steps:

1. The detection of regions with increased brightness (higher intensity);
2. The isolation of profiles which the human eye recognizes as shadow.

STEP 1: The detection of regions with increased brightness (higher intensity)

Since the images obtained in Vigo and Braga come from different equipment, was firstly calculated to each image its dimensions and its center (by dividing both the size in x and in y by 2) to establish the first standard to normalize the processing.

Then, and intending to analyze intensity variations in the images, these were converted from RGB code to grey scale (pixel normalization from 0 to 255 levels of grey) using the rgb2gray function.

Posteriorly, was necessary a conversion from cartesian coordinates to polar coordinates (figure 5.9) because the images were acquired radially and the software by default assumes the bottom left corner as the starting point to process pixel by pixel.

Originally, polar coordinates regard the following trigonometric equations:

$$\begin{cases} x = r \cos (\varphi) \\ y = r \sin (\varphi) \end{cases} \text{ where } r = \sqrt{x^2 + y^2}, r \geq 0 \text{ and } \varphi \in [-\pi, \pi]$$

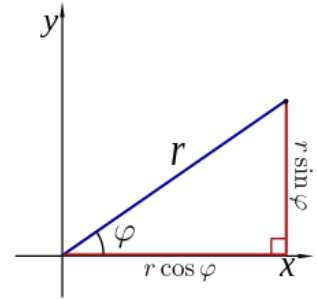


Figure 5.9: Polar coordinates

This formulation is correct considering x and y initially equal to 0, but in the case of the analyzed images, the original values of x and y are defined by the coordinates of the center of the image ($center_x$ and $center_y$). So, to take this in consideration the equations were adapted as follows and a new axle system, presented in figure 5.10, was implemented:

$$\begin{cases} x = center_x + r \cos (\theta) \\ y = center_y - r \sin (\theta) \end{cases} \text{ where } r = \sqrt{x^2 + y^2}, r \geq 0 \text{ and } \theta \in [0, 2\pi]$$

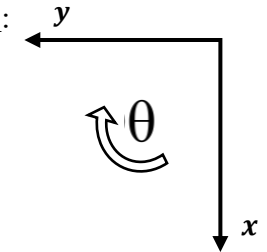


Figure 5.10: Implemented axle system

In order to analyze the image radially and trace a profile intensity for each line, it is necessary for each angle variation (radians) obtain the maximum number of r values and the intensity for each one of the values. Initially, a degree variation of 0.1° was considered, meaning the image was separated in steps of 0.1 degrees, equivalent to 3600 profiles of intensity $\left(\frac{360^\circ}{0.1}\right)$.

Considering a 1024×1024 image, and dividing it radially as mentioned before with a maximum radius of 512 pixels, and using a degree variation of 0.1° , is obtained a p value ($p = 512 \times \sin 0.1$), presented in figure 5.11, of 0.89 pixels. Meaning that this degree variation of 0.1° represents an approximate resolution of 1 pixel.

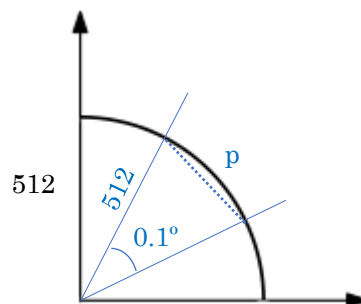


Figure 5.11: Schematic of degree variation and pixel resolution

The algorithm performs this analysis through a *for* cycle where, in the end, the maximum value taken by r is the radius of a circumference that is contained inside a square with the size of the image. Also, a matrix is filled with the maximum value taken by r (r_{max}) columns and a number of lines according to the analyzed degree variation. The formula used to convert degrees in radians is the following: $var_{angle} = \frac{(variation\ degree=0.1) \times \pi}{180^\circ}$.

The schematic presented in figure 5.12 illustrates the areas which are analyzed, and the ones left out starting from the center of the image, proving the excluded areas do not contain relevant information for the analysis of the image.

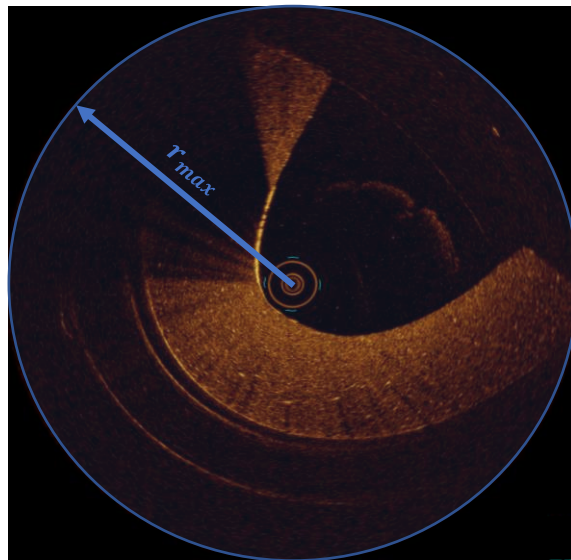


Figure 5.12: Schematic of the analyzed areas by the algorithm (blue) and the ones excluded (black) maintaining the same number of columns in the matrix

The obtained matrix traces the intensity profile of each line and each value of intensity is obtained by intersecting the value of r with the angle. After having a complete matrix (example of an image acquired in Hospital de Braga where each image has 1024 x 1024 pixels and with a degree variation of 0.1 = obtained matrix M (3600,512)) is calculated the maximum intensity value present with max function.

After the maximum intensity value of the analyzed image is obtained, the profiles containing points with a range of 95% to 100% of the maximum intensity are isolated and saved in a different matrix. This parameter can be later be adjusted by the user (for further information please read User's Interface Guide). With this filter the step 1 of the algorithm is complete and it is possible to start step 2. The main goal of step 2 of the algorithm is to distinguish profiles like the ones presented in Figure 5.13 where an increased brightness is verified but only one of them presents a shadow.

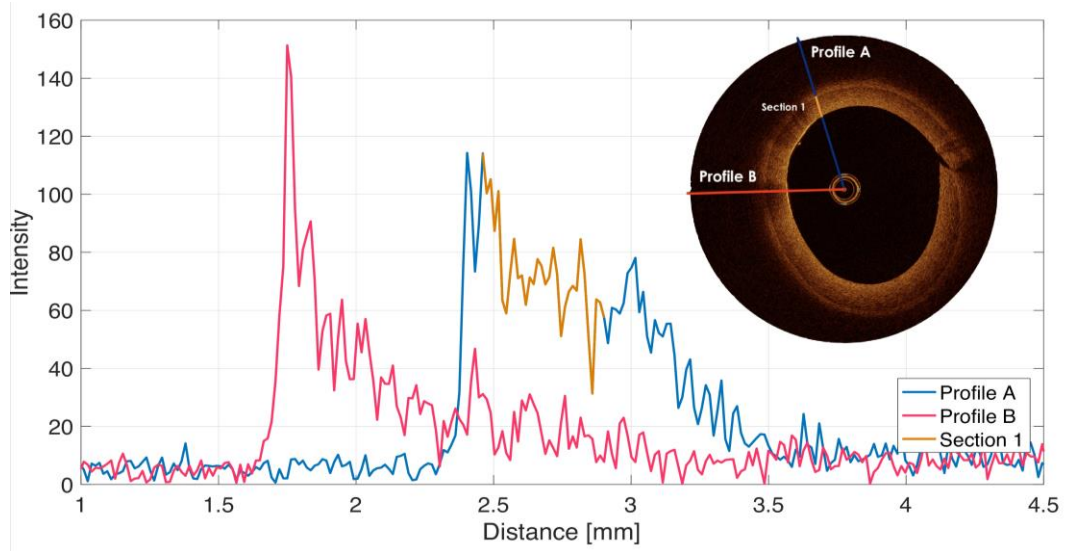


Figure 5.13: Comparison between 2 types of profiles. Profile A presenting a homogenous distribution of scattering and profile B presenting a shadow and a well-defined intensity peak

STEP 2: The isolation of profiles which the human eye recognizes as shadow

According to the last image presented (Figure 5.13) it is crucial to distinguish each of the profiles that present increased intensity values, relatively to the remaining image, have in fact a shadow or an absence of bright nearby. As so, the next filter applied consisted in the evaluation of the number of peaks in each profile using the function `findpeaks`, which returned parameters like the number of peaks, the intensity and the location of each peak.

More importantly, was the use of the parameter `minPeakHeight` which established the condition of only analyzing the peaks which had minimum 90% of the highest intensity of the profile. Meaning that, it was only analyzed the profiles which had a very well-defined peak and it were excluded the peaks that had similar intensities and occurred in higher number.

A new matrix was created including only the lines of the profiles which fulfilled every requirement presented above. Also, one of the observable characteristics of the profiles of interest is the fact that both before and after the peak the average of intensity is considerably lower than the maximum intensity peak value.

The profiles translate the location of regions of interest that may contain valuable information for future diagnosis. Figure 5.14 represents the difference between two profiles, where one represents the location of a contrast agent, where a very well-defined peak is observed, and the other a generic region of the sample.

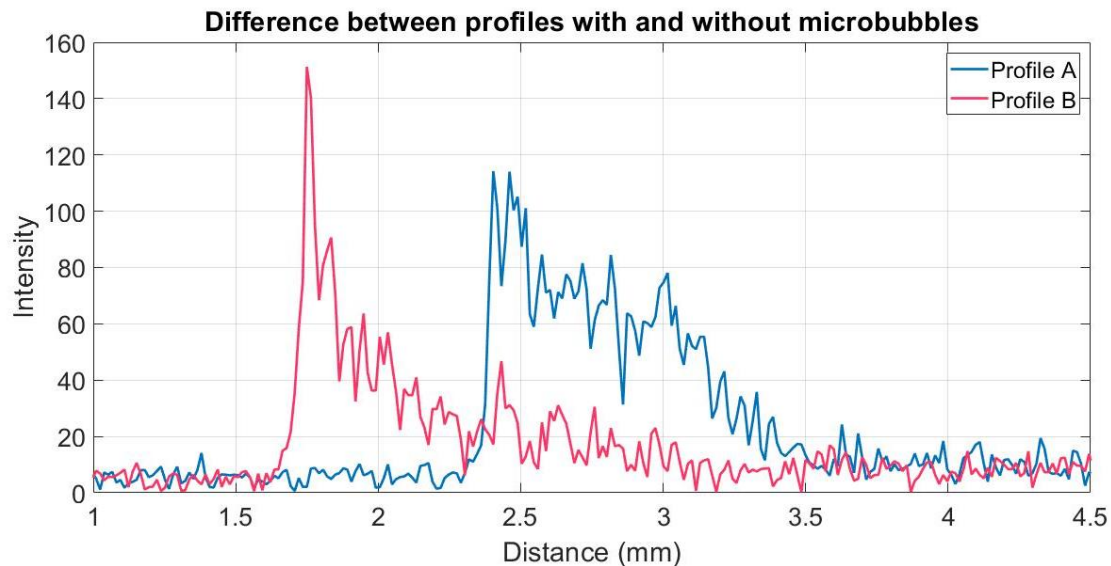


Figure 5.14: Difference in profiles where Profile A represents a generic region and Profile B represents the location of a contrast agent

To be possible for the user to interact with the developed algorithm was simultaneously developed an interface, also using MATLAB software, which allowed both automatically and manually detect regions of interest. When the user decides to use a manual mode for the detection it is possible to replace 3 of the parameters presented above: the degree variation (by default 0.1), the range of maximum intensity analyzed (by default 0.95) and the minimum peak height of the profile (by default 0.9).

It was developed, as a tool of the main Interface, an auxiliary interface (REFERENCE_AREA INTERFACE) that contained reference images used in the medical community to realize current diagnosis. The images used were based on the OCT Compendium[19] used by cardiologists worldwide.

A User's Guide is also provided as an appendix of the document as a tutorial of use of both the main and the auxiliary interface.

5.3 Accuracy tests

Tests with the interface were performed to validate the accuracy of the algorithm both in phantoms and arteries. Alongside with the algorithm to detect regions of interest was developed another algorithm to correctly trace lines that delimitate the region of interest. Since it was established a new axial system, different trigonometric equations need to be taken in consideration when the detected angles were inferior and superior to 180 degrees.

Considering that the algorithm only detects one or zero regions of interest, it will be detected a maximum of 2 values of degrees. If it is detected one region of interest, to trace both lines, are necessary three pairs of coordinates:

- [x1 y1] that establish the point where the line starts, and it is equal for both the detected angles;
- [x2 y2] that establish the point where the line ends for the first detected angle;
- [x3 y3] that establish the point where the line ends for the second detected angle.

The first pair of coordinates [x1 y1] corresponds to the center of the image in the axes x and y. Then the second pair of coordinates [x2 y2] is obtained in function of the first detected degree (variable *init_degree*) which is initially converted to radians and the maximum considered radius (r_{max}) of the image. If the initial degree is higher than π then the values of x2 and y2 are calculated using the following considerations:

$$\begin{cases} x2 = x1 + r_{max} \times (\sin(\text{init_degree} - \pi)) \\ y2 = y1 - r_{max} \times (\cos(\text{init_degree} - \pi)) \end{cases}$$

Otherwise, if the initial degree is lower than π then the values of x2 and y2 are calculated using the following considerations:

$$\begin{cases} x2 = x1 - r_{max} \times (\sin(\text{init_degree})) \\ y2 = y1 + r_{max} \times (\cos(\text{init_degree})) \end{cases}$$

Similarly, the third pair of coordinates [x3 y3] is obtained with the same considerations but replacing the value of the (*init_degree*) for the value of the second detected angle (variable *final_degree*).

Firstly, it was assured that in calibration images were not displayed any lines to delimitate regions and the number of regions of interest appears as zero, as presented in figure 5.15.

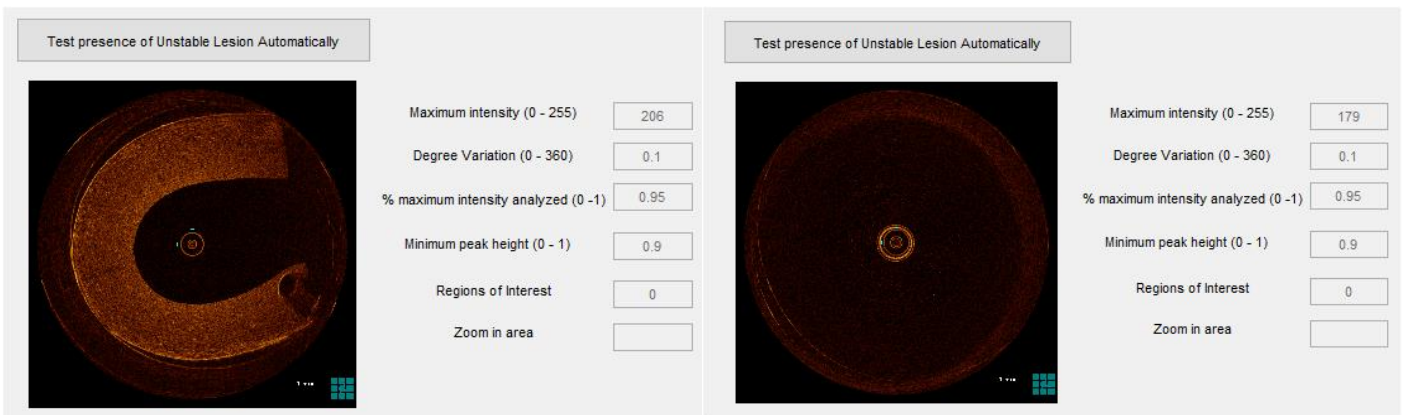


Figure 5.15: Detection of regions of interest in calibration measurements. Phantom without microbubbles (left) and water (right).

After assuring that calibration measurements were correctly identified in the algorithm, tests started to be performed in phantoms. Figure 5.16 presents the first example of the correct delimitation (lines in blue) of the region of interest using a phantom's image.

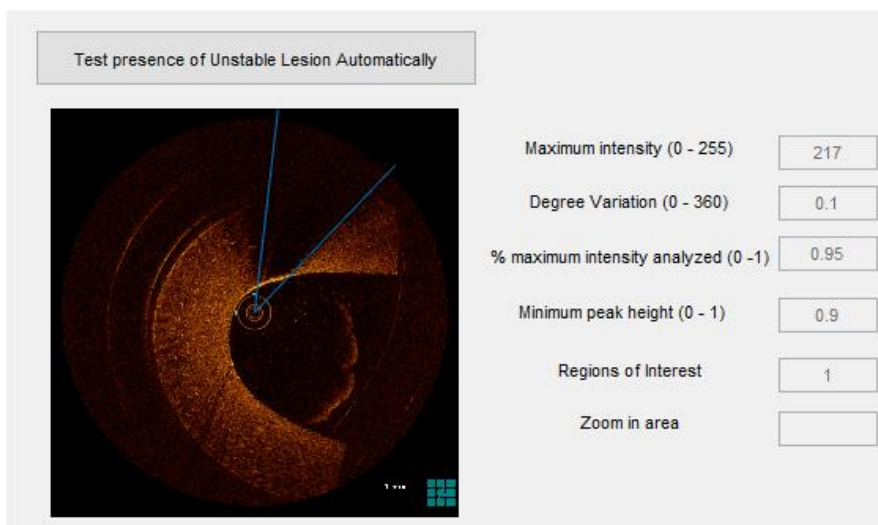


Figure 5.16: Correct detection of region of interest in phantom

A second image of a phantom was also tested but a less successful result was obtained. The algorithm was only capable of detecting partially the region of interest. This partial detection occurred due to a breach in the deposition of the microbubbles causing a significant loss of signal in the region. Figure 5.17 presents the detection performed by the algorithm (in blue) and the zoom in the image showing the occurrence of a breach. The green dashed line represents the limit that the algorithm should have detected if the breach didn't exist.

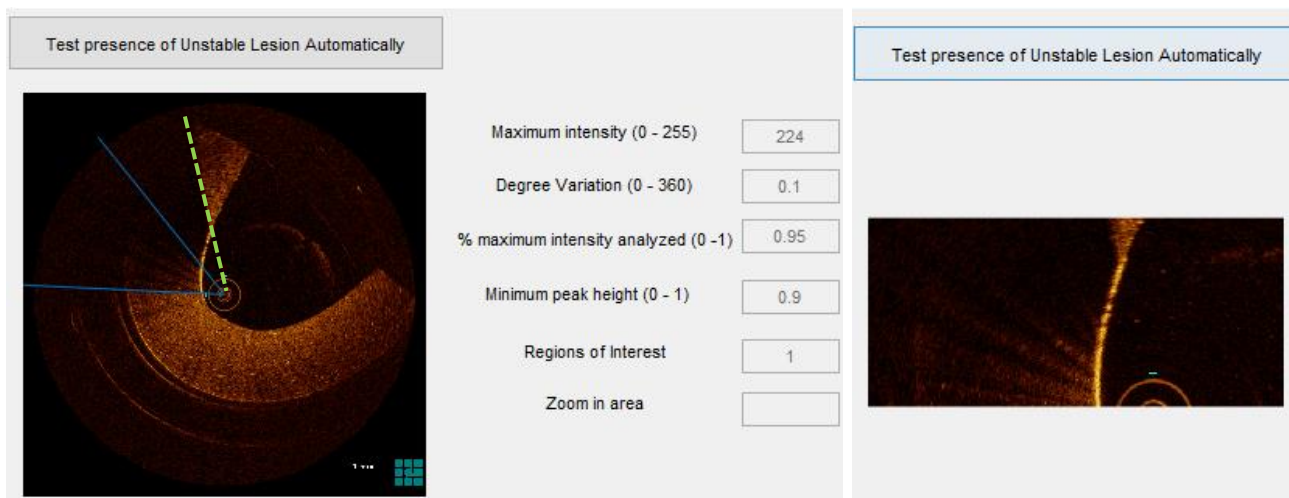


Figure 5.17: Partial detection of region of interest in phantom (left) and zoom in the breach (right)

This limitation may be exceeded by creating a range of degrees (for example 10) where the algorithm continues to run even if finds a gap of intensity. Meaning that, if the decrease of intensity is only detected in a gap of 10 steps (in 3600 steps by default) and after this time the algorithm detects again the same value of intensity as before the gap, it ignores the gap and considers the region as one. Although this method wasn't fully implemented, figure 5.18 shows that if the image mentioned before didn't contain a breach the algorithm would be fully functional.

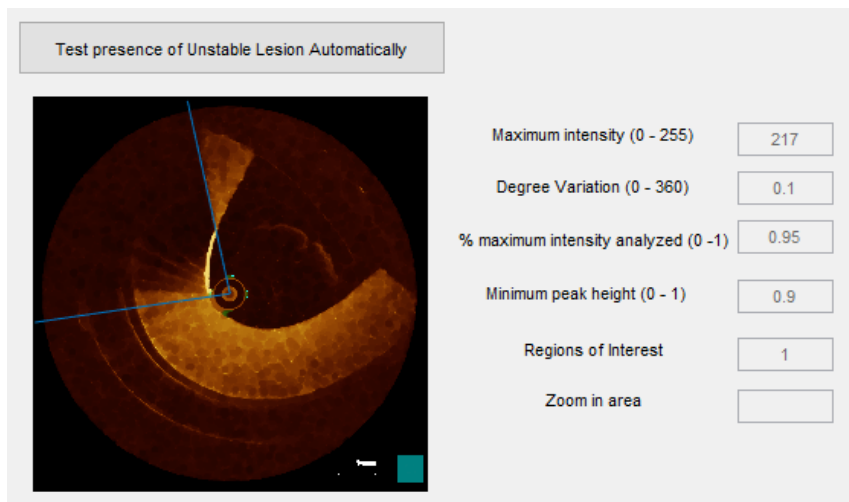


Figure 5.18: Correct detection of region of interest in phantom after eliminating the pre-existing breach

Posteriorly, were performed the same tests in images of human arteries also marked with microbubbles. Although the results weren't as correct as in phantoms it is visually easy to understand that arteries have much more complicated anatomies and it is not as clear what are the regions of interest. Figures 5.19 and 5.20 presents some cases with arteries. The green dashed line represents where the limit of the region should end.

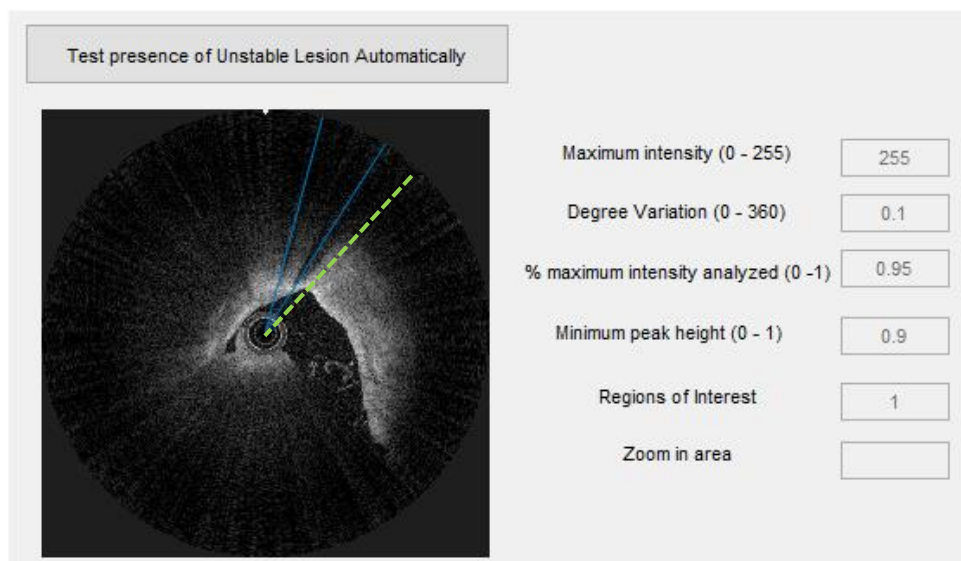


Figure 5.19: Partial detection of region of interest in human artery

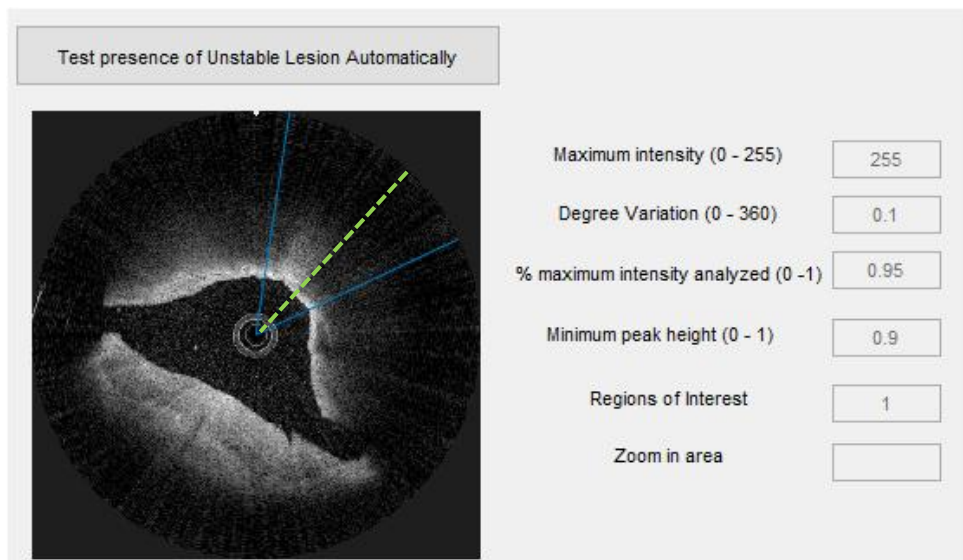


Figure 5.20: Partial detection of region of interest in human artery

Finally, figure 5.21 presents a case where the algorithm is unable to detect any region of interest. Although the region is hard to detect visually it is expected in the future the algorithm to detect hard cases like this one.

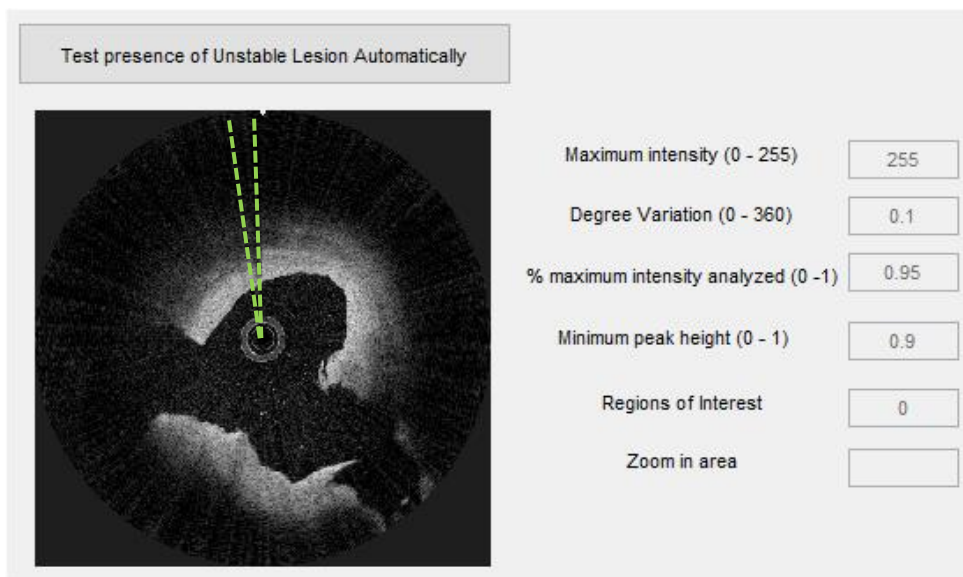


Figure 5.21: Incorrect detection of region of interest in human artery

6. Conclusions

The work developed throughout this thesis has proven the applicability of microbubbles, in a range of 1.2 to 1.5 μm of diameter (functionalized and up to 3 μm non functionalized), as contrast agents in intravascular optical coherence tomography (IV-OCT) images. Comparison with gold nanostars with an average diameter of 55 nm as contrast agents was performed and verified a higher contrast in images presenting microbubbles.

Microbubbles placed on the surface of single and double layered PDMS phantoms containing titanium dioxide (TiO_2) as a scatterer were used to replicate the behavior of human arteries to infrared light. PDMS higher affinity to microbubbles to maintain them at the surface of the phantom, its malleability and ease of access as well as the use of different concentrations of TiO_2 to reproduce the scattering of different tissues, confirms the need of using phantoms to optimize OCT measurements before stepping into postmortem arteries.

To confirm the use of microbubbles as contrast agents, besides the successful measurements of the location of the contrast agent in IV-OCT images of phantoms, images with human arteries were acquired. Microbubbles marked with antibodies recognizing endothelial cells were injected in postmortem arteries and a higher contrast followed by a shadow was observed in the intima, where endothelial cells are located, providing a positive confirmation that microbubbles fit as localizers of specific types of cells.

The precise location of the contrast agent in the OCT images was obtained by developing an analysis software with a user-friendly interface in MATLAB. The software analyzes the image and identifies the regions with higher contrast followed by a shadow, as a region of interest where the microbubbles are probably located. Then presents several analyzed parameters: maximum intensity peak detected, number of regions of interest detected, variation degree (meaning which interval was used between the analyzed profiles), percentage of maximum intensity in order to isolate areas with the highest peaks of intensity, minimum peak height to isolate the profiles that presented a shadow.

A manual detection of regions of interest was also possibly by the modification of the last three parameters present above. The interface also allows the user to modify basic parameters in the OCT image like brightness, contrast and gamma at the same time that analyzes the histogram of the processed image. A parallel interface was also developed with reference images, accessed in the main interface by a button, in case the user has doubts of the image that is currently analyzing.

In future research, more specific functionalization methods need to be applied to the microbubbles in order to recognize not endothelial cells, but inflammation markers present when the atherosclerotic lesion is ready to prone and is considered unstable. Additionally, more precise measurements of the microbubbles' concentration used to achieve the best contrast enhancement need to be performed. Also, it will be necessary to figure out how to use functionalized microbubbles in the PDMS phantoms. Besides, the streptavidin-biotin bond works perfectly in laboratorial medium, but it cannot be used in the human body due to the non-specificity of the biotin with the blood components.

Regarding the analysis software, an optimization in the isolation of the profiles of interest by analyzing a higher number of parameters like, width to half height of each peak, first derivative and signal-to-noise ratio. Also, an improvement of the algorithm to identify more than one region of interest, which is particularly interest when analyzing images of postmortem arteries. Additionally, produce quality tests on the software using more images of postmortem arteries in order to assure the accuracy of the software. Finally, converting the MATLAB script to an open source and more robust programming language will be necessary when producing the final product to be delivered in hospitals and clinics.

With the aim that in the future is possible to distinguish the nature of atherosclerotic plaques, identify each ones are ready to prone and consequently prevent a cardiac event, I consider this thesis has presented significant advances since it has identified a contrast agent that can be used with no harm in the human organism but also provides a clear identification of its location in the OCT images.

References

- [1] M. Varna, H. V. Xuan, and E. Fort, “Gold nanoparticles in cardiovascular imaging,” *Wiley Interdiscip. Rev. Nanomedicine Nanobiotechnology*, vol. 10, no. 1, p. e1470, Jan. 2018.
- [2] R. Virmani, A. P. Burke, F. D. Kolodgie, and A. Farb, “Vulnerable Plaque: The Pathology of Unstable Coronary Lesions,” *J. Interv. Cardiol.*, vol. 15, pp. 439–446, 2002.
- [3] F. Otsuka, M. Joner, F. Prati, R. Virmani, and J. Narula, “Clinical classification of plaque morphology in coronary disease,” *Nat. Publ. Gr.*, vol. 11, no. 7, pp. 379–389, 2014.
- [4] C. C. Oliviera and M. Brito, “How to Look Closely to Vulnerable Atherosclerotic Plaques using Nanoparticles,” *J. Nanomedicine Res.*, vol. 6, no. 1, 2017.
- [5] A. S. Kini *et al.*, “Fibrous Cap Thickness by Optical Coherence Tomography In Vivo,” *J. Am. Coll. Cardiol.*, vol. 69, no. 6, 2017.
- [6] L.-C. Engel *et al.*, “Novel Approach for In Vivo Detection of Vulnerable Coronary Plaques using Molecular 3-T CMR Imaging with an Albumin-Binding Probe,” *JACC Cardiovasc. Imaging*, 2018.
- [7] I. Porto, A. Mattesini, S. Valente, F. Prati, F. Crea, and L. Bolognese, “Optical coherence tomography assessment and quantification of intracoronary thrombus: Status and perspectives,” *Cardiovasc. Revascularization Med.*, vol. 16, no. 3, pp. 172–178, 2015.
- [8] R. S. Fenning and R. L. Wilensky, “New insights into the vulnerable plaque from imaging studies,” *Curr. Atheroscler. Rep.*, vol. 16, no. 3, pp. 1–9, 2014.
- [9] Y. Ponce De León, J. L. Pichardo-Molina, N. Alcalá Ochoa, and D. Luna-Moreno, “Contrast enhancement of optical coherence tomography images using branched gold nanoparticles,” *J. Nanomater.*, 2012.
- [10] J. Hu *et al.*, “Dynamic single gold nanoparticle visualization by clinical intracoronary optical coherence tomography,” *J. Biophotonics*, 2017.
- [11] D. Singh, S. Singh, J. Sahu, S. Srivastava, and M. R. Singh, “Ceramic nanoparticles : Recompense , cellular uptake and toxicity concerns,” vol. 2262832, no. August 2014, pp. 401–409, 2016.
- [12] H. Assadi, V. Demidov, R. Karshafian, A. Douplik, I. A. Vitkin, and Homa, “Microvascular contrast enhancement in optical coherence tomography using microbubbles,” *J. Biomed. Opt.*, vol. 21, no. 7, p. 075003, 2016.
- [13] R. K. Manapuram, V. G. R. Manne, and K. V. Larin, “Phase-sensitive swept source optical coherence tomography for imaging and quantifying of microbubbles in clear and scattering media,” *J. Appl. Phys.*, vol. 105, no. 10, 2009.
- [14] M. Borden and S. Sirsi, “Microbubble Compositions, Properties and Biomedical Applications (For types of microbubble shells),” *Bubble Sci Eng Technol.*, vol. 1, pp. 3–17, 2010.
- [15] M. B. Cardiovascular, “Targeting of microbubbles - contrast agents for ultrasound molecular imaging,” vol. 26, pp. 420–434, 2019.
- [16] A. Taki, A. Kermani, S. M. Ranjbarnavazi, and A. Pourmodheji, *Overview of Different Medical Imaging Techniques for the Identification of Coronary Atherosclerotic Plaques*, 1st ed. Elsevier Inc., 2016.
- [17] G. Van Soest, L. Marcu, B. E. Bouma, and E. Regar, “Intravascular imaging for

- characterization of coronary atherosclerosis,” *Curr. Opin. Biomed. Eng.*, vol. 3, pp. 1–12, 2017.
- [18] V. Tuchin, “Tissue Optics and Photonics: Light-Tissue Interaction II,” *J. Biomed. Photonics Eng.*, vol. 2, no. 3, p. 030201, 2016.
- [19] H. Nef and A. Elsasser, *OCT Compendium*. 2016.
- [20] C.-É. Bisailon, M. L. Dufour, and G. Lamouche, “Artery phantoms for intravascular optical coherence tomography: healthy arteries,” *Biomed. Opt. Express*, vol. 2, no. 9, p. 2599, 2011.
- [21] P. Koczera *et al.*, “PBCA-based polymeric microbubbles for molecular imaging and drug delivery,” *J. Control. Release*, vol. 259, pp. 128–135, 2017.
- [22] M. H. Jazayeri, H. Amani, A. A. Pourfatollah, H. Pazoki-Toroudi, and B. Sedighimoghaddam, “Various methods of gold nanoparticles (GNPs) conjugation to antibodies,” *Sens. Bio-Sensing Res.*, vol. 9, pp. 17–22, 2016.
- [23] G. Chirico, P. Pallavicini, and M. Borzenkov, “Physical properties of gold nanostars,” in *Gold Nanostars: Synthesis, Properties and Biomedical Application*, 2015.
- [24] D. P. Popescu *et al.*, “Optical coherence tomography: Fundamental principles, instrumental designs and biomedical applications,” *Biophys. Rev.*, vol. 3, no. 3, pp. 155–169, 2011.
- [25] F. Prati *et al.*, “Expert review document on methodology, terminology, and clinical applications of optical coherence tomography: Physical principles, methodology of image acquisition, and clinical application for assessment of coronary arteries and atherosclerosis,” *Eur. Heart J.*, vol. 31, no. 4, pp. 401–415, 2010.
- [26] P. H. Tomlins and R. K. Wang, “Theory, developments and applications of optical coherence tomography,” *Journal of Physics D: Applied Physics*. 2005.
- [27] P. Serranho, A. M. Morgado, and R. Bernardes, “Optical Coherence Tomography: A Concept Review,” 2012.
- [28] *et al.* Janeway CA Jr, Travers P, Walport M, “Immunobiology: The Immune System in Health and Disease. 5th edition. T-cell receptor gene rearrangement.,” *New York Garl. Sci.*, 2001.
- [29] V. Rai and N. Dey, “The Basics of Confocal Microscopy,” *Laser Scanning, Theory Appl.*, pp. 3–5, 2012.
- [30] U. Maver, T. Velnar, M. Gaberšček, O. Planinšek, and M. Finšgar, “Recent progressive use of atomic force microscopy in biomedical applications,” *TrAC - Trends Anal. Chem.*, vol. 80, pp. 96–111, 2016.
- [31] L. Reimer, “Scanning Electron Microscopy: Physics of Image Formation and Microanalysis, Second Edition,” *Meas. Sci. Technol.*, 2002.
- [32] Science Education Resource Center - Carleton University, “Geochemical Instrumentation and Analysis - Scanning Electron Microscopy.” [Online]. Available: https://serc.carleton.edu/research_education/geochemsheets/techniques/SEM.html. [Accessed: 11-Jun-2019].
- [33] G. Lamouche *et al.*, “Review of tissue simulating phantoms with controllable optical, mechanical and structural properties for use in optical coherence tomography,” *Biomed. Opt. Express*, vol. 3, no. 6, p. 1381, 2012.
- [34] J. Turkevich, P. C. Stevenson, and J. Hillier, “A study of the nucleation and growth processes in the synthesis of colloidal gold,” *Discussions of the Faraday Society*. 1951.
- [35] T. Hendel, M. Wuithschick, F. Kettemann, A. Birnbaum, K. Rademann, and J. Polte, “In situ determination of colloidal gold concentrations with uv-vis spectroscopy: Limitations

and perspectives,” *Anal. Chem.*, 2014.

Appendix I – User’s Guide

The interface developed during this project is a tool to process intravascular cardiologic images acquired with an OCT equipment. The purpose of developing a user’s guide for the interface is to document the functionalities provided by the software as well as the possibilities of interaction with the user.

Firstly, an overall view of the interface is presented in figure I.1, where it is possible to visualize 3 main areas:

- one area to adjust basic parameters of the image, like brightness, contrast and gamma and visualize the effect on a histogram;
- another area to test automatically the existence of regions of interest as well as the parameters used in the algorithm to process the image or manually insert the parameters of interest;
- lastly an area that generates an automatic report with the parameters used to process the image.

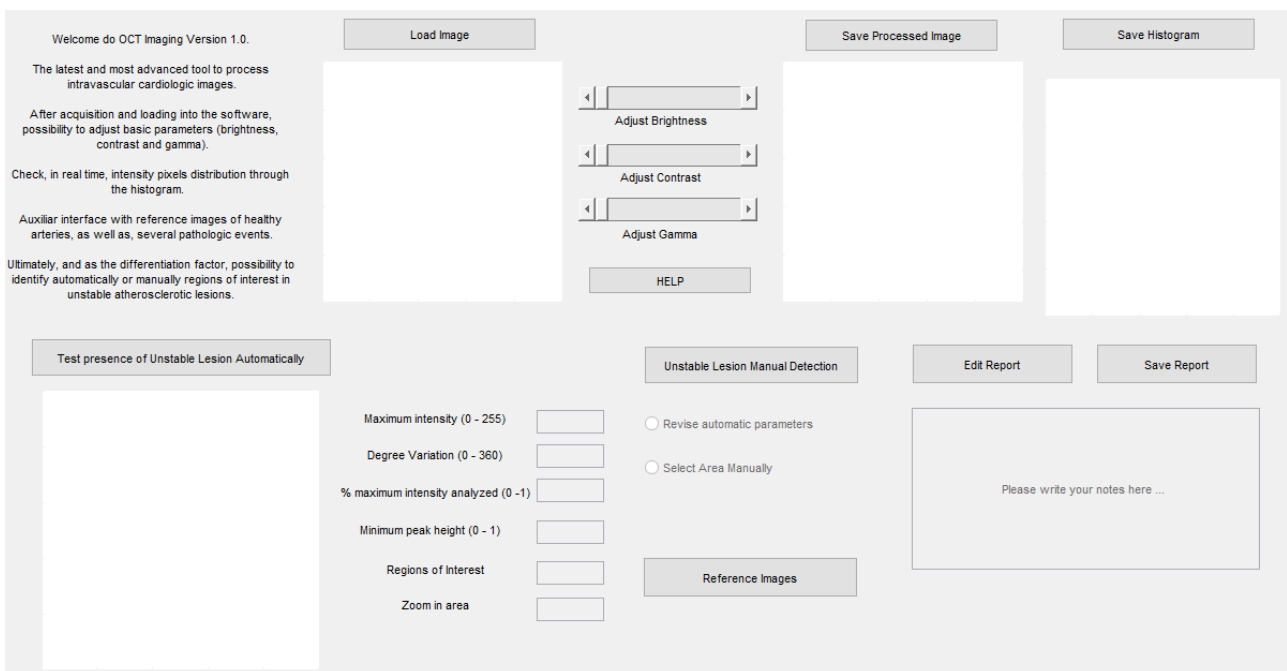


Figure I.1: Overall view of the interface

First, the user presses the *Load Image* button and chooses the image that would like to process from a range of types of files (.png, .jpg, and .bmp). Then decide if wants to adjust the basic parameters of the image or to test automatically the existence of regions of interest.

In case the user decides for the first option, has the possibility to adjust 3 parameters: brightness, contrast and gamma. Figure I.2 will consider the original image and the histogram of reference.

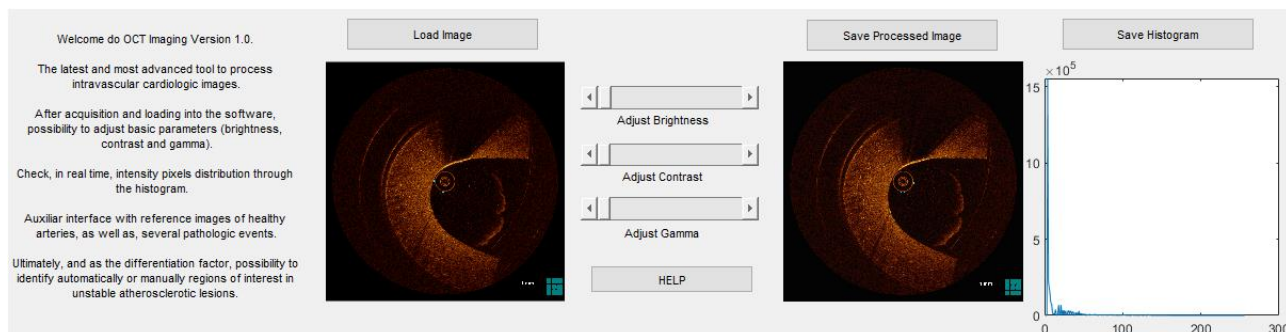


Figure I.2: Original image and corresponding histogram of reference

Then, the images presented below will show the following effects on the histogram of the loaded image:

- Increase brightness, the image becomes more intense and the histogram is displaced right (pixels intensity become closer to 255) – figure I.3;

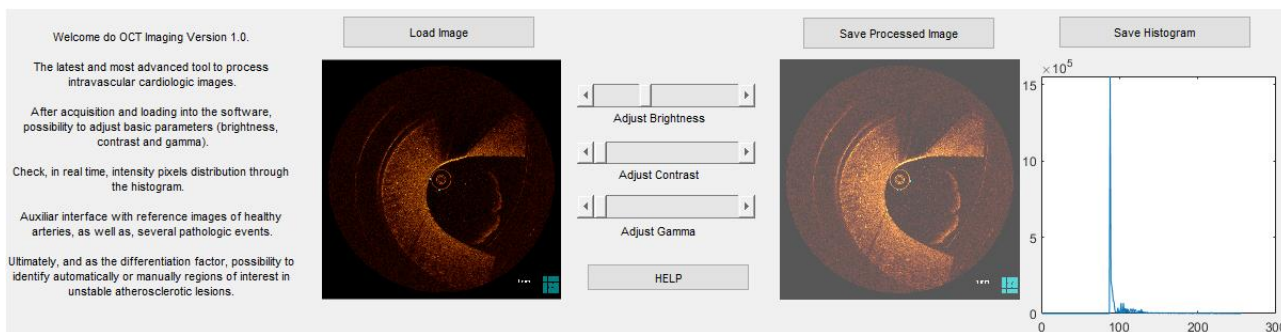


Figure I.3: Processed image with increased brightness and corresponding histogram

- Decrease brightness, the image becomes darker and the histogram is displaced left (pixels intensity become closer to 0);
- Increase contrast, the difference of intensity between the pixels of the image becomes more visible and the intensity values appear more spread in the histogram – figure I.4;

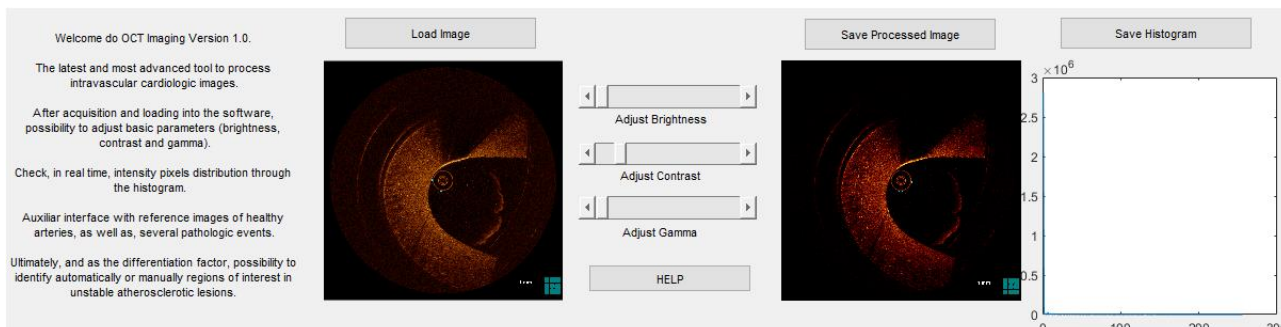


Figure I.4: Processed image with increased contrast and corresponding histogram

- Decrease contrast, the difference of intensity between the pixels of the image becomes less visible and the histogram appears denser;
- Gamma < 1, the contrast increases in the dark areas and decreases in the bright ones and the evidences on the histogram aren't easy to detect because the relation is not linear – figure I.5;

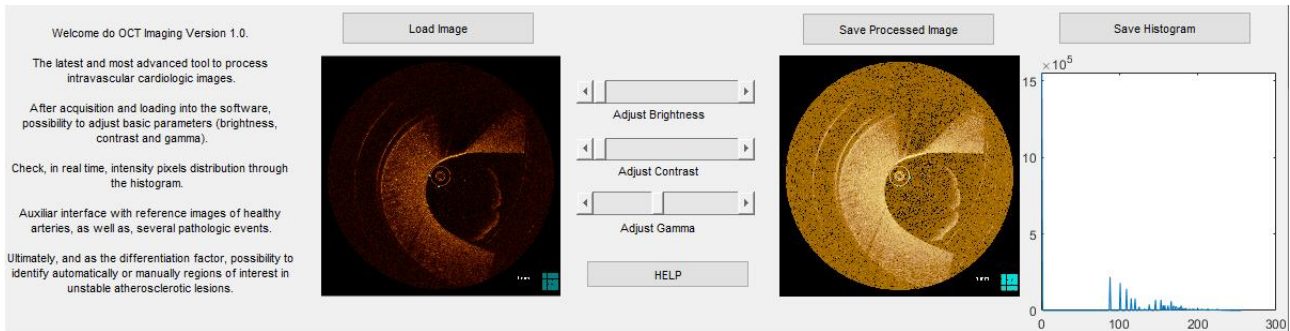


Figure I.5: Processed image with gamma < 1 and corresponding histogram

- Gamma > 1, the contrast increases in the bright areas and decreases in the dark ones and the evidences on the histogram aren't easy to detect because the relation is not linear.

After processing and adjusting basic parameters of the image it's time to test automatically the existence of regions of interest. By pressing the button *Test presence of Unstable Lesion Automatically*, the algorithm presented in chapter 5 analyzes the loaded image previously. If the algorithm detects any region of interest 2 blue lines will appear in the image setting out the boundaries of the region. Also, the parameters used to run the algorithm (maximum intensity value detected, degree variation used, percentage of the maximum intensity analyzed, minimum peak height) will be presented as well as the number of regions of interest detected (in case any region is detected blue lines will not appear and the number of regions of interest is 0). Figure I.6 shows both cases presented above.

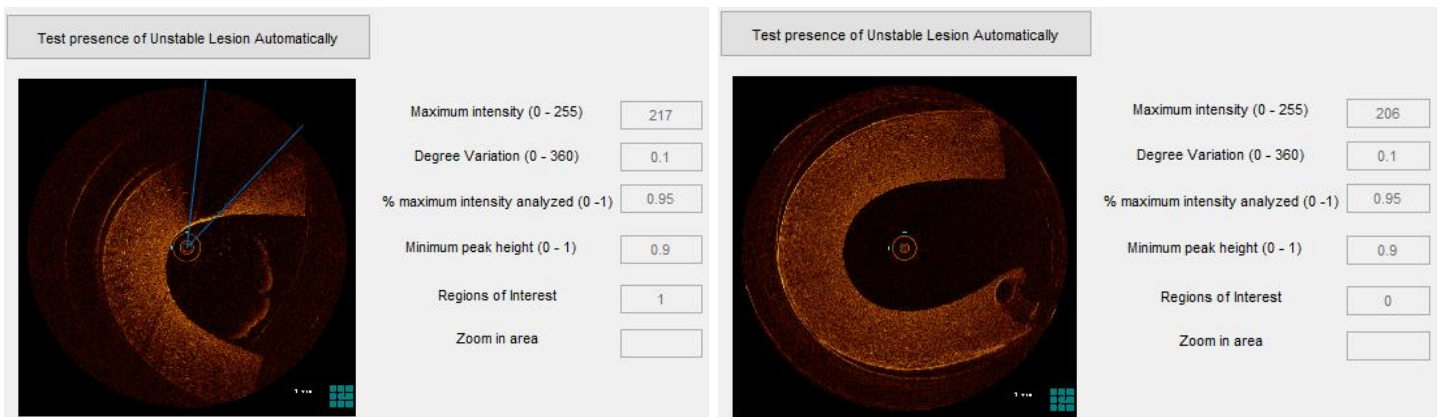


Figure I.6: Automatic detection of regions of interest (1 – left and 0 right)

Until this point, all the parameters editor boxes are disabled and are only accessible when the user presses the button for the manual detection of regions of interest *Unstable Lesion Manual Detection*. After pressing this button, the user has the option of altering only 3 of the 5 presented parameters (degree variation, percentage of the maximum intensity analyzed and minimum peak height) since the maximum intensity value is a property of each image and the number of regions of interest is updated every time the algorithm runs the image. To choose this option the user should press the radio button *Revise Automatic Parameters*, as presented in figure I.7.

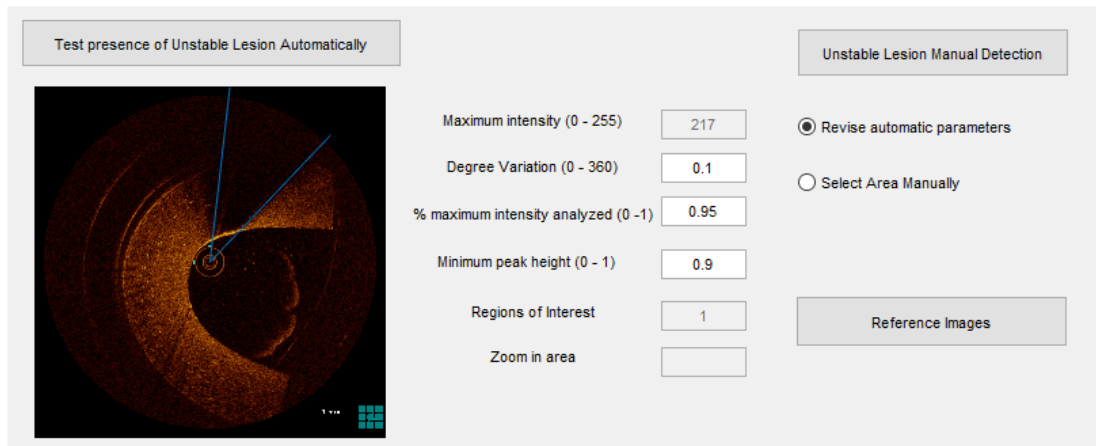


Figure I.7: Activation of editable parameters by manual detection

The user has also the possibility to zoom in a specific area of the image by pressing the radio button *Select Area Manually*. The value of the selected area will also appear on the interface above the number of regions of interest detected, as presented in figure I.8.

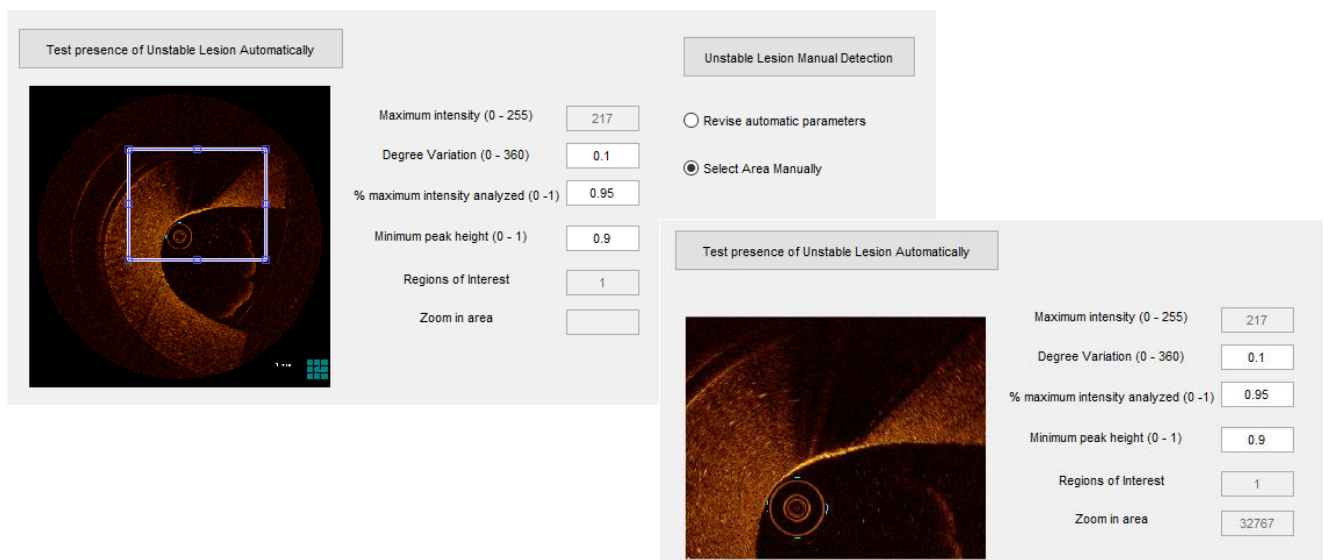


Figure I.8: Example of a crop and zoom in the analyzed image

In order to provide the best support to the most accurate diagnosis was simultaneously developed an auxiliary interface *Reference Images*, which contains images of reference of both healthy and pathological arteries. The images presented in the interface were not acquired during the project but were provided by an OCT Compendium[19] used in clinical practice.

The interface contains images of a healthy artery, stable fibrous plaque, thin cap fibrous atheroma (TCFA), thick cap fibrous atheroma (ThCFA), plaque rupture, thrombus and stent, as presented in figure I.9.

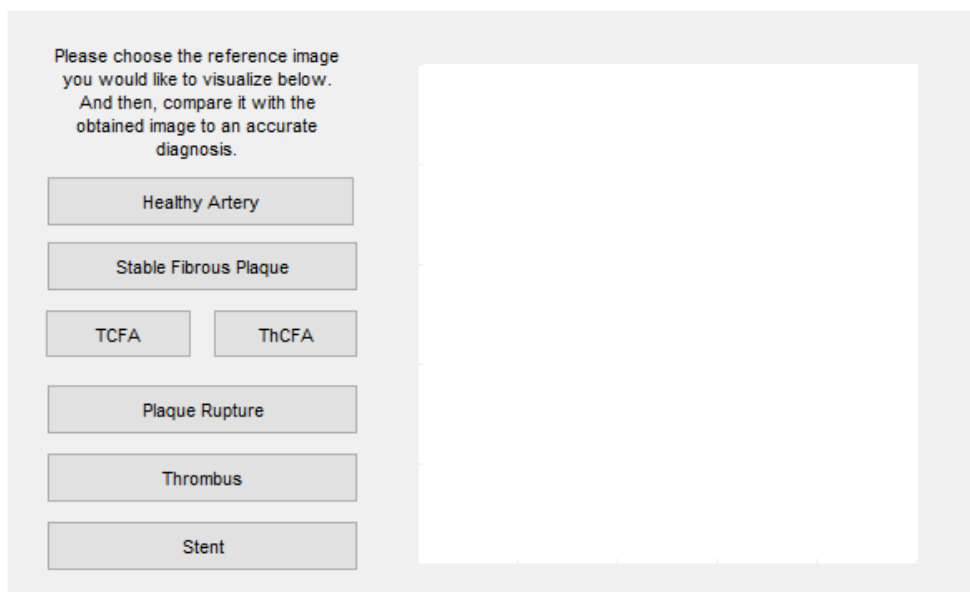


Figure I.9: Overall view of the auxiliary interface for reference

After choosing the reference image, a pop-up message appears on the screen with an explanation of the image and some of the characteristics of the pathology in study. Figure I.10 presents an example of the pop-up of an image of a plaque rupture.

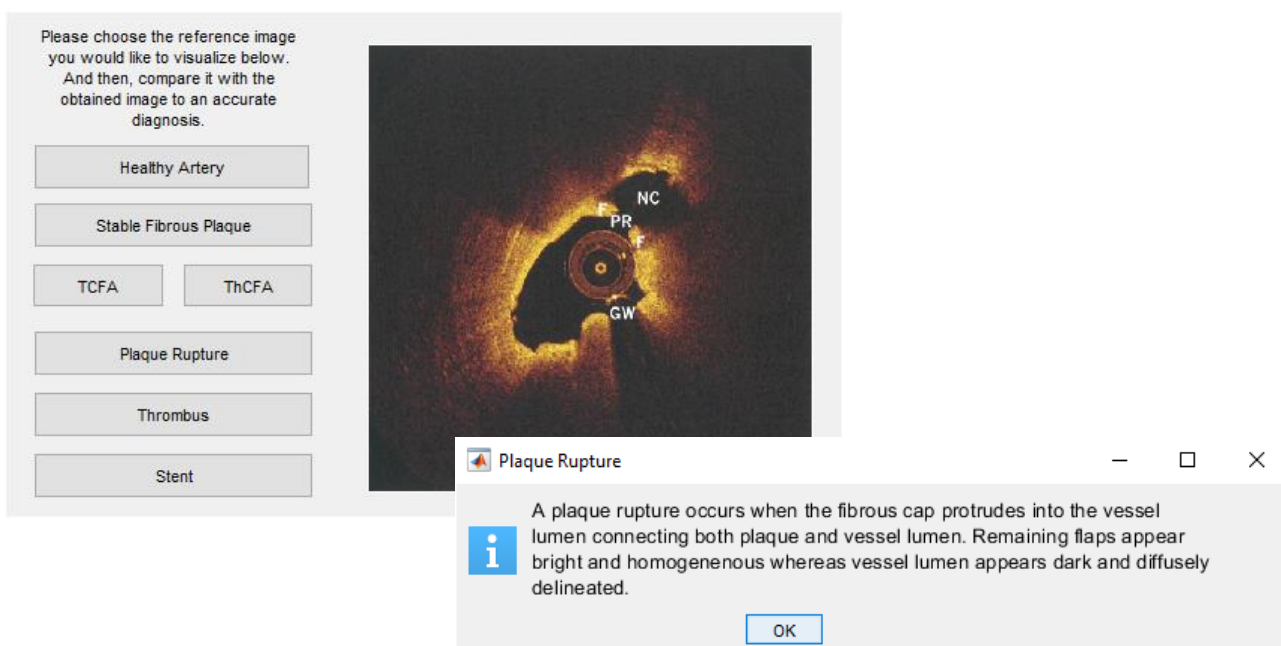


Figure I.10: Pop up message and corresponding reference image

Finally, and after the acquisition of all the parameters of the analyzed image, a report is automatically generated by pressing the *Edit Report* button. The report contains the values of maximum intensity value detected, degree variation used, percentage of the maximum intensity analyzed, minimum peak height and regions of interest previously calculated by the algorithm. It is also possible to save this report using the *Save Report* button in a .txt file. Figure I.11 presents that values appearing in the report are the ones calculated previously by the algorithm.

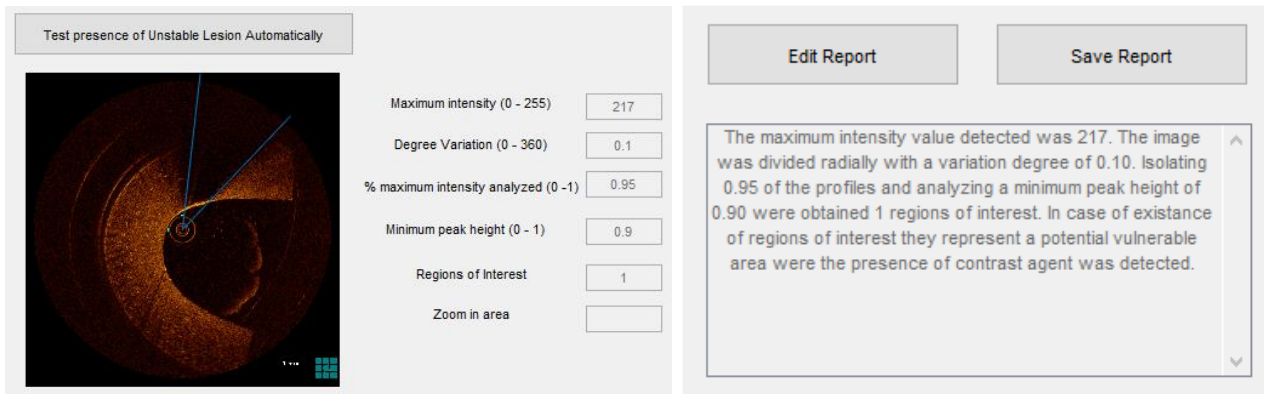


Figure I.11: Report generated after running the algorithm